Acta Materialia 225 (2022) 117551

Contents lists available at ScienceDirect

Acta Materialia

journal homepage: www.elsevier.com/locate/actamat

Full length article

Measurement of the single crystal elasticity matrix of polycrystalline materials

Paul Dryburgh*, Wenqi Li, Don Pieris, Rafael Fuentes-Domínguez, Rikesh Patel, Richard J. Smith, Matt Clark

Optics and Photonics Group, University of Nottingham, University Park, Nottingham, NG7 2RD, UK

ARTICLE INFO

Article history:
Received 22 September 2021
Revised 21 November 2021
Accepted 7 December 2021
Available online 20 December 2021

Keywords:
Elastic constants
Surface acoustic waves
Material characterization
Laser ultrasound
Crystalline orientation

ABSTRACT

Many engineering metals are polycrystalline, as such the elasticity, crystalline orientation and grain distribution are cardinal factors in determining the physical properties of the material. The grain distribution can be measured using a number of different techniques and the orientation by a subset of these (electron back scatter diffraction, spatially resolved acoustic spectroscopy). These measurements are routinely deployed in materials development. However, the elasticity remains a more difficult parameter to measure and is rarely measured because the existing techniques are slow and cumbersome, with most current techniques requiring the laborious growth or destructive isolation of single crystals. In this work we present a technique that can determine the elasticity, crystalline orientation and grain distribution in a fast and easy measurement. The technique utilises SRAS imaging to provide the raw measurement of single grain velocity surfaces, this is input to a novel inverse solver that mitigates the problem of the inversion being very ill-conditioned, by simultaneously solving for multiple uniquely orientated grains at once in a brute-force approach. This allows simultaneous determination of the elastic constants and crystallographic orientation. Furthermore, this technique has the potential to work on polycrystalline materials with minimal preparation and is capable of high accuracy, with the potential to realise errors in the determination of elastic constants values of less than 1 GPa (~ 1). In this work we demonstrate good agreement with EBSD ($< 6^{\circ}$ disagreement on average for all Euler angles) and determine elastic constants in line with existing single-crystal values, with an expected accuracy of better than 4 GPa. Experimental results are presented for pure α-Ti (hexagonal), Ni and the more exotic Ni-base alloy CMSX-4 (both cubic). With the proposed method, once the initial measurement has been made, subsequent measurements of the elasticity on the same sample can be made rapidly so that the elasticity can be measured in real time, opening the possibility that on-line measurement of elasticity can be used to monitor processes and enable high-throughput materials screening. The current instrumentation approach is applicable to materials with grain sizes down to 50 µm, with the possibility of improving this to grain sizes of ~ 5 µm. Further modifications to instrumentation and acoustic velocity calculation will facilitate greater accuracy in the determination of elastic constants.

1. Introduction

Many engineering materials form, when in the solid state, into a crystalline structure. The lack of rotational symmetry in such crystal lattices imparts direction specific properties (these can be mechanical, electrical and optical) on to the crystal; this is known as anisotropy. The elastic constant tensor of the material provides an essential understanding of the materials response to external stresses in the elastic regime. It would be difficult to overstate the importance of the elastic constants to understanding the behaviour of a material. Fundamentally, the elastic constants relate stress to strain [1], and provide a bridge between the micro- and macroscopic worlds. From an engineering perspective, knowledge of the elastic constants and orientation in anisotropic crystalline materials is vital for understanding the in-service mechanical performance and facilitates the calculation of engineering elastic parameters including: Voigt's modulus, Reuss's modulus, Hill's modulus, shear modulus, Young's modulus, bulk modulus, Poisson's ratio, and unveils other physical properties including strength, hardness, wear and melting temperature [2]. For the materials scientist, measured elastic constants can communicate information on many

* Corresponding author.
E-mail address: paul.dryburgh@nottingham.ac.uk (P. Dryburgh).

https://doi.org/10.1016/j.actamat.2021.117551

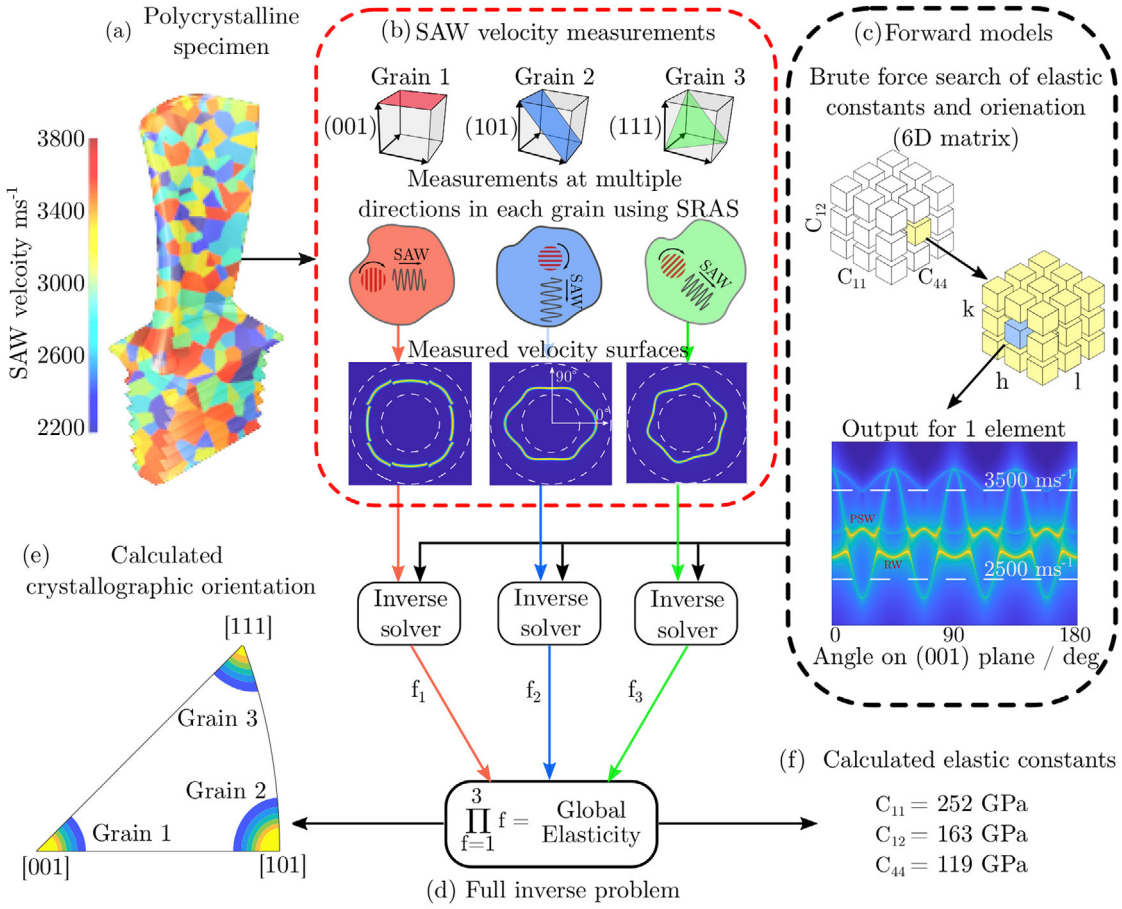

Fig. 1. The new inversion method described in this work, detailing the process of calculating the crystallographic orientation and elastic constants for a synthetic specimen. (a) The SAW velocity is measured in multiple grains using spatially resolved acoustic spectroscopy. By rotating the generation patch velocity surfaces can then be built up for each grain. The velocity surfaces shown are from three arbitrary planes of nickel (here we use three primary planes as examples). (c) The forward model is searched for the range of possible elastic constants (C_{11}, C_{12}, C_{44}) and crystalline orientation (hkl). Each element of the forward model determines the velocity of all SAWs, which can propagate across that plane. (d) The output of the forward model search and one experimentally measured velocity surface are input to the inverse solver. The inverse solver calculates the 'goodness of fit' between the velocity surface and each element of the forward model. This is then repeated for each measured grain before taking the product of the figure of merit for all grains. The specimens elastic constants are then determined by the location of the maxima. (e) Calculated crystallographic orientation from the inverse solver, showing the three grains on one pole figure. (f) Final calculated elastic constants for this specimen. The figure shows three grains being used but the general algorithm is applicable to any number of velocity surfaces, results are improved when the orientation space will well sampled.

important phenomena in solids including magnetic and electron-lattice interactions, phase-transitions and mode softening [3]. In short, elastic constants have an essential role to play in the calculation of many key physical quantities and in turn our wider understanding of materials on the whole.

The term single-crystal elastic constants refers to the values that describe single orientation grain behaviour, in contrast to the values that represent the bulk behaviour of aggregate media often calculated through Voigt-Reuss-Hill averaging. To date, determination of single crystal elastic constants has primarily been achieved by ultrasonic measurement, mechanical testing to sample the compliance tensor or theoretical calculation from first principles. Given that the longitudinal wave velocity is a function of C_{ijkl} and ρ, all ultrasonic measurements are in some sense probing the elasticity of the material. Fig. 1 conveys the link between the three factors (i) acoustic velocity (ii) elastic constants and (iii) crystallographic orientation, whereby normally two are needed to calculate the third. This approach is exploited throughout our engineered world, from medical imaging to seismology.

Primarily the need to measure the elastic constants is driven by the evolution of material processing techniques and novel alloy development. However, the progress in measuring techniques has fallen out-of-step with the rate of development in materials. This has resulted in a situation where the majority of techniques for determining the elastic constants are only viable with single crystals specimens. However, it is infeasible for the vast majority of compounds to be grown into single-crystals, making such techniques unsuitable. Du and Zhao estimated that this applies to around 99% of the possible 160,000 distinct solid compounds, in addition to many solid-solution compounds used in common structural alloys [4]. Additionally, the proliferation of powder-feedstock additive manufacturing techniques has opened the door to easy in-situ alloying, allowing new alloys to be created rapidly [5]. In such cases, the elastic constants for the pure element are used, often resulting in significant errors in the calculated mechanical properties.

In addition to growing single crystals, traditional ultrasonic techniques have required the resulting crystallographic orientation to be a favourable plane for inversion, such that an analytical solution can be found [6]. More recent developments have enabled elastic constants to be extracted from polycrystalline specimens in limited cases, usually assuming an orientation distribution is perfectly random or highly textured [7], and with over 1000 grains such that small deviations from individual grains can be suppressed [8]. Most real specimens live in the intermediary, exhibiting a weak texture and not enough grains to make such assump-

tions on the statistical properties. In short, bulk-wave measurements can provide excellent sensitivity, but without good knowledge of the internal microstructure are fundamentally limited to working on single-crystal materials. Although it is worth noting Lan et al. [9] and Tant et al. [10] did provide inverse techniques that recover some of the internal microstructure orientation from bulk wave measurements, this may provide a basis for determination of elastic constants in the future. Relevant acoustic techniques for determining crystallographic orientation or elastic constants are summarised in Appendix A (Table A.2).

Surface acoustic waves (SAWs) are a good candidate for characterising polycrystalline specimens, as they allow acoustic localisation - allowing the properties of each grain to be probed separately. Aside from a few primary planes, analytical solutions for SAWs are not tractable [11]. Thus, numerical schemes are a requisite for orientation and elastic constant inversion. However, authors such as Xu et al. have concluded common optimisation algorithms such as Powell's method are ill-suited to the elastic constants problem and do not reliably determine the true values [12].

Aside from ultrasonic methods, nanoindentation modulus measurement, coupled with orientation measurement have recently been applied to obtain orientation-dependent Young's modulus. Whilst this method has not yet demonstrated the capability of evaluating the full elastic constant values, there is no reason why this is not feasible [13]. Atomic force microscopy (AFM)-based methods are well-established for the elasticity measurement of biological specimens, producing extremely high spatial resolution qualitative modulus maps. However, extraction of accurate elastic constants is still far from a reality, especially for hard materials such as metals [14]. Scattering of neutrons and x-rays have also previously been used to determine elastic constants. Whilst the accuracy of these techniques is relativity poor compared to the approaches already presented, it has allowed elastic constants to be determined at extremely high temperatures [15] and in difficult to handle elements, such as barium [16].

A list of experimentally measured elastic constants in pertinent materials (including those determined in this work) are available in Appendix B, highlighting the variation in elastic constants reported for many materials. Ledbetter and Reed suggested this was less a symptom of poor measurement accuracy than a failure to rigorously characterise the materials studied [17]. Variations in the measured elastic constants can be a function of chemical impurities, residual stress, processing route and magnetic saturation.

The present study proposes that starting from the SAW velocity it is possible to simultaneously determine the crystalline orientation of each velocity surface and the elastic constants of the specimen as a whole. Refinements in the forward model have allowed a quasi brute-force approach to the inversion to be executed for the first time, overcoming many of the issues with previous numerical inversion schemes. When coupled with the practically simple ultrasonic technique spatially resolved acoustic spectroscopy (SRAS), elastic constants can be reliably determined from specimens with arbitrary crystalline orientation with good agreement to existing single-crystal values. This method is particularly applicable to polycrystalline specimens to realise three clear benefits: the (often laborious) process of producing a single crystal is not required; the crystallographic orientation does not need to be known or lend itself to analytic inversion; and allows the properties of materials in-service to be captured directly in the specific specimen, as opposed to using facsimiles.

This paper is structured as follows, in Section 2, we begin by introducing the numerical underpinning of the study, and detailing the experimental system used in this work. In Section 3, we explore the sensitivity of SAW to changes in the elastic constants and the resulting solution space, relating the expected error in elastic constant determination to the measurement error of the experimental system. In Section 4, experimental results in single crystal Ni, polycrystalline CMSX-4 and α-titanium are presented, we compare and discuss all experimental measurements in relation to validation measurements. Finally, in Section 5, we discuss implications of the proposed methodology and opportunities for future improvements, before concluding.

2. Methodology and materials

2.1. Inversion algorithm

The general method outlined in this work can be explained by providing a worked example, outlined in Fig. 1, before discussing each component in detail. (a) Starting with a polycrystalline specimen of unknown elastic constants and crystalline orientation, using spatially resolved acoustic spectroscopy (SRAS) the surface acoustic wave velocity (SAW) is captured across the specimen in multiple propagation directions (b). The measurements from three of the grains are shown as radial velocity surfaces, note the different wave modes and velocities on each plane. Fig. 1(c) The possible velocity surfaces for each elastic constant permutation and crystalline orientation is then determined using a brute-force search of the forward model. The forward model looks for solutions to the Christoffel equation by scanning for roots of the determinant. Several wave modes, including the Rayleigh (RSAW) and pseduo (PSAW) surface waves, can be seen to propagate on this plane - each plane is a single element of the forward model solution (§2.2 details the forward model for calculating the SAW phase velocity). Fig. 1(d) Each element of the forward model is then compared to the measured velocity surfaces, using the overlap function as the inverse solver (§2.3 details the overlap function and inversion process). Each grain input then produces an independent figure of merit for the elasticity and orientation space. By assuming that the elastic constants are a global property of the specimen, the elasticity figures of merit for each grain can be combined to give a final set of elastic constants for the full specimen. Finally, the orientation of each grain is then recalculated using the determined elastic constants. Fig. 1(e) Figure of merit for orientation space, showing the orientation goodness of fit for grains 1, 2 and 3.

This approach can be formalised by Eq. (1), where: Ng is the number of grains measured; F_{EO} is the elasticity-orientation figure of merit for each of these grains; $\overline{F_E}$ is the ensemble elasticity figure of merit for the whole specimen; (hkl) and ϕ_1 denote the modelled plane and rotation; and C_{ij} is the modelled elastic constant matrix. The orientation with the greatest correlation value is selected for each element of C_{ij}. The elastic constants derived from $\overline{F_E}$ are then substituted back in to each F_{EO} to determine the correct orientation in each grain. A full list of symbols is given in Appendix C.

$$\begin{aligned}\overline{F_E}(C_{ij}) &= \prod_1^{N_g} F_{EO}(C_{ij}, W, X, Y, Z) \\ &\quad (W(C_{ij}), X(C_{ij}), Y(C_{ij}), Z(C_{ij})) \\ &= \underset{(h,k,l,\phi_1)}{\arg\max}\, F_{EO}(C_{ij}, h, k, l, \phi_1).\end{aligned} \tag{1}$$

2.2. Forward model

To calculate the SAW velocity for a given orientation and elasticity, the elastic wave equation must be solved with appropriate boundary conditions. An elastic wave propagating on a surface with normal x_i exerts a stress, T_{ij}, in the axis x_j. From Hooke's law T_{ij} can rewritten in terms of elasticity and strain, giving the elastic wave equation in anisotropic media, Eq. (2). ρ is the material density, u_i the displacement in the x_i axis and C_{ijkl} is the materi-

als fourth-rank elasticity stiffness tensor. This formalises the relationship between crystallographic orientation, elasticity and SAW propagation. It is important to note other effects, such as temperature and residual stress can either change the values of C_{ijkl} or the boundary conditions, usually these effects are vanishingly small compared to the variations to anisotropy.

$$\rho \frac{\partial^2 u_j}{\partial t^2} = C_{ijkl} \frac{\partial^2 u_k}{\partial x_i \partial x_l} \text{ for i,j,k,l} = 1, 2, 3. \tag{2}$$

The solution of the wave equation, Eq. (2), is:

$$u_i = \alpha_i \exp\left(jk[l_1 x_1 + l_2 x_2 + l_3 x_3 - vt]\right) \tag{3}$$

substituting Eq. (3) into Eq. (2) gives a set of homogeneous equations, the well-known Christoffel equation, Eq. (4). For non-trivial solutions the determinant of the Christoffel equation must equal zero. This approach is the standard operation for the calculation of acoustic wave velocities. For known elastic constants the bulk wave velocities may be found simply by finding the roots which satisfy a non-zero determinant.

$$(C_{ijkl} l_i l_j - \rho v^2 \delta_{ik})\alpha_k = 0 \text{ for i,j,k,l = 1,2,3} \tag{4}$$

For SAWs the boundary conditions, in addition to the wave equation, must also be satisfied. Firstly, As $x_3 \to -\infty$ then the displacement must vanish, that is to say the displacement decreases when moving away from the free surface.

We may assume the solution of the wave equation for is a linear combination of the terms of the form of Eq. (3), with each having the same phase velocity, v, but an l_3 value equal to one of the three lower half plane roots of Eq. (4). The solution is then given by Eq. (5).

$$u_i = \sum_{n=1}^{3} C_n \alpha_i^{<n>} \exp\left(jk[l_1 x_1 + l_2 x_2 + l_3^{<n>} x_3 - vt]\right) \tag{5}$$

C_n is the weighting factor corresponding to the eigenvector, $\alpha_i^{<n>}$ of the root $l_3^{<n>}$, which is a solution to the Christoffel equation. A zero-traction boundary must also exist at $x_3 = 0$, giving the boundary condition of Eq. (6).

$$T_{3j} = C_{3jkl}\epsilon_{kl} = 0, \qquad \text{at } x_3 = 0, \qquad \text{for j = 1,2,3} \tag{6}$$

Thus, the problem is then to determine the weighting factors, (C_1, C_2, C_3), of Eq. (5) such that the boundary conditions are satisfied. Substituting the assumed solution, Eq. (5), into the boundary conditions, Eq. (6), gives rise to another 3×3 equation set - we may call this the Rayleigh boundary value matrix, R. Again the determinant of this set of equations must be zero for a non-trivial solution, $\Delta R = 0$. The members of R may be found by Eq. (7).

$$r_{nm} = C_{m3kl} \alpha_k^{<n>} l_l^{<n>} \tag{7}$$

True surface wave solutions exist when the Rayleigh determinant, ΔR, equals zero. In addition, pseudo-surface waves (PSAW) can exist with non-zero determinant, which can only satisfy the boundary conditions by shedding energy in the form of a bulk wave which leak into the solid. PSAWs can therefore only propagate with attenuation, nevertheless along certain directions on specific planes these waves are observed in preference to true surface waves. This set of non-linear equations can not be solved analytically (expect in certain high symmetry directions) and it is necessary to search numerically for minima in the value of the ΔR, as proposed by Farnell [18]. Fig. 1(c) shows the value of ΔR for (a) the (001) plane in nickel. At certain propagation directions four distinct modes can exist simultaneously: RSAW, PSAW and the fast and slow transverse waves.

One known drawback of the forward solver is the calculation of the dominant modes. Currently the solver discriminates from the theoretical displacement of each mode. However, this is an imperfect model as it does not account for the generation mechanism. Some of the possible wave modes are inefficiently generated by thermoelastic absorption. Veres et al. have been able to implement this to good effect by finite difference modelling [19]. Where possible, we have omitted measurement points close to the transition, so as to prevent this artefact from dominating the inversions reported in this work.

The elasticity tensor C_{ijkl} can be written as the 2D matrix C_{ij} in Voigt notation, where the crystal symmetry determines the number of independent constants. For example, Eq. (8) shows the 2D representation of the cubic and hexagonal stiffness matrices, with three and five unknown constants, respectively, for example in the cubic case $C = C(C_{11}, C_{12}, C_{44})$.

$$C_c = \begin{bmatrix} C_{11} & C_{12} & C_{12} & 0 & 0 & 0 \\ C_{12} & C_{11} & C_{12} & 0 & 0 & 0 \\ C_{12} & C_{12} & C_{11} & 0 & 0 & 0 \\ 0 & 0 & 0 & C_{44} & 0 & 0 \\ 0 & 0 & 0 & 0 & C_{44} & 0 \\ 0 & 0 & 0 & 0 & 0 & C_{44} \end{bmatrix}$$

$$C_h = \begin{bmatrix} C_{11} & C_{12} & C_{13} & 0 & 0 & 0 \\ C_{12} & C_{11} & C_{13} & 0 & 0 & 0 \\ C_{13} & C_{13} & C_{33} & 0 & 0 & 0 \\ 0 & 0 & 0 & C_{44} & 0 & 0 \\ 0 & 0 & 0 & 0 & C_{44} & 0 \\ 0 & 0 & 0 & 0 & 0 & C_{66} \end{bmatrix} \tag{8}$$

where $C_{66} = (C_{11} - C_{12})/2$.

Considering a cubic structure, the forward model calculates the SAW velocity along each plane between the principle planes (001), (101), (011) and (111) at rotations between 0 and 180°, thus the theoretical velocities are defined as $v(\text{h,k,l}, \phi_1)$.

In the case of a hexagonal structure, the plane and rotation are defined by the Euler angles ϕ_1 and Φ, where ϕ_1 is the rotation on the plane and Φ is the plane (0° is the basal plane). Therefore, the theoretical velocities are defined as $v(\Phi, \phi_1)$. The Euler angle ϕ_2 cannot be determined by linear acoustic techniques [20].

2.3. Overlap function

The process of determining the orientation and/or elastic constants from the SAW velocity is not straight forward. If two of the orientation, velocity or elastic constants are known, then, in principle, the third can be computed. However, determining either physical parameter from the velocity is an ill conditioned problem that does not lend itself to a tractable analytical solution [21]. The presence of experimental noise makes the direct inversion impractical and unreliable. Instead, the authors have previously proposed the process of calculating the overlap between the forward model and experimentally measured velocity surfaces. The full experimentally measured velocity surface spectrum is used for the inversion, this is unlike most schemes, which use just the single velocity measurement [22]. This approach was found to be more robust to experimental noise and a reduced number of scanned directions. Notations in this section refer to the cubic case, references to (hkl) are substituted for Φ when dealing with hexagonal materials [20]. For simplicity, we initially describe the method of calculating only the crystallographic orientation (elastic constants are known) from the measured SAW velocity.

The velocity spectrum of a given propagation direction is found by taking the fast Fourier transform of the measured signal acoustic (see Section 2.5 for greater detail). For each pixel in the specimen, the acoustic measurement provides a plot of signal amplitude against velocity as a function of propagation direction, θ, this is the velocity surface spectrum (example of velocity surfaces for the planes (001), (101) and (111) in nickel are shown in Fig. 1b).

Therefore, the measured signal can be defined as $A(v(h,k,l,\phi_1),\theta)$, where $0^\circ \leqslant \phi_1 < 180^\circ$.

The experimental dataset described above must then be compared to the velocity database calculated from the forward model, $v_c(h,k,l,\phi_1)$. The forward modelled calculated velocity must be assembled into an analogous dataset of amplitude against propagation direction. To achieve this, the SAW velocity, as calculated by the forward model, is transformed into a binary matrix I_{hkl} by Eq. (9) (this takes values of SAW velocity calculated by the forward model and creates a map of amplitude against prorogation direction, the map is zero at all points expect the velocity index corresponding to the forward model value). I_{hkl} has the same velocity dimension, N_v, as measured signal A (which varies depending on the zero-padding in Fourier transform), and is twice the length of A in the rotation dimension - this allows the rotation of A relative to the forward model to be determined.

$$I_{hkl}(v,\phi_1) = \begin{cases} 0, & v \neq v_c(h14k,l,\phi_1) \\ 1, & v = v_c(h,k,l,\phi_1) \end{cases} \tag{9}$$

The overlap between I_{hkl} (forward model output) and A (measured experimental data) is now determined by calculating the sum of the element-wise product as the lag of I_{hkl} (with respect to A) is varied, as defined by Eq. (10).

$$\begin{aligned} S_{hkl}(p,q) = \sum_{v=1}^{N_v}\sum_{\theta=1}^{180} A(v,\theta) I_{hkl}(v-p,\theta-q) \\ -(N_v-1) \leqslant p \leqslant N_v - 1 \\ -360 < q < 360 \end{aligned} \tag{10}$$

The v index in the result, S, represents a velocity offset, that is to say making the measured wave linearly faster or slower. However, the velocity measured by the experimental system has already been calibrated we therefore assume these is not systematic offset in the measured velocity and therefore only $p = 0$ is of interest. The q value reflects the rotation of the measured data relative to the $\phi_1 = 0^\circ$ definition in the forward model, this can again be limited to the range $-180^\circ < q < 180^\circ$, outside of this range the velocity surfaces do not fully overlap and a maximum should not be found.

The value of the figure of merit F_O for this orientation is then found by Eq. (11), where S_{hkl} is the output of Eq. (10) for a given plane (hkl). The process described thus far has evaluated the overlap function, S, for a single crystallographic plane; to determine the crystallographic orientation the overlap function is evaluated for all planes (as calculated by the forward model) - the result of the inversion is then the crystallographic plane (h,k,l) and rotation (ϕ_1) which has maximised the value of F_O. This summarises the method of calculating the crystallographic orientation from the measured SAW velocity.

$$F_O(h,k,l,\phi_1) = S_{hkl}(\phi_1) \tag{11}$$

Similarly, when solving for unknown elastic constants (but a known orientation), the figure of merit is given by Eq. (12), where $S_{C_{ij}}$ is the output of Eq. (10) for a given elastic constant set at a single orientation.

$$F_E(C_{ij}) = S_{C_{ij}}) \tag{12}$$

Thus far in this section we have described the overlap function for determining crystallographic orientation or elastic constants. In the case that neither are known, as is the thrust of this work, Eq. (10) is repeated for every modelled elastic constant set and orientation (as neither are known), thus the figure of merit for the full inverse problem is $F_{EO}(C_{ij},h,k,l,\phi_1)$, for a single pixel.

2.4. Simulation

As described by Smith et al., the error of a SRAS measurement may be described by the standard deviation of the measured SAW velocity. These fluctuations from the true velocity cause errors in the described inversion process and it is important to correlate the measurement error to the error in the elastic constant determination. As such, a simple process was established to simulate experimental measurements, as a function of the velocity standard deviation.

Starting with a predetermined 'correct' velocity surface (taken from the forward model), the 180 (or fewer) velocity measurements around the plane, v, are perturbed by a small velocity, δv. This process produces a final velocity surface which mimics the experimental measurement. This process can be be shown by Eq. (13).

$$v + \delta v = v_{\text{measured}} \text{ where } \delta v \sim \mathcal{N}(0,\sigma_v^2). \tag{13}$$

$\mathcal{N}(0,\sigma_v^2)$ is a normal distribution, of mean 0 and a variance of σ_v^2. The value of v_{measured} is then interrogated for a standard deviation of the velocity error, σ_v between 0 and $1000\,\text{ms}^{-1}$. This spans the currently achievable standard deviation in the measured SAW velocity [23]. Finally, using Eq. (13), 1000 velocity surfaces are generated for each value of σ in order to sufficiently sample the normal distribution of velocity perturbations. Results from this method are discussed in Fig. 6.

2.5. Experimental set-up

Spatially resolved acoustic spectroscopy (SRAS) is well established for determining the crystallographic orientation in a variety of crystalline materials by measuring the SAW velocity across the specimen in multiple propagation directions. However, it relies on knowledge of the elastic constant values, as taken from existing literature, to generate the forward models for the orientation inversion [24]. Diagrams of the experimental system used in this work and the generation phenomena are shown in Fig. 2(a) and (b), respectively.

SRAS utilises a short pulse ($\sim 1\,ns$, 2 kHz repetition rate) Q-switched laser to generate surface acoustic waves (SAWs). The Q-switched laser is used to illuminate an optical mask, which is then re-imaged on to the specimen surface, Fig. 2(a). This structured light is absorbed and through the thermo-elastic effect, creates a surface acoustic wave. The grating fringes imaged on the specimen surface typically have a spacing of $24\,\mu m$ (as used in this work), which directly corresponds to the wavelength of the SAW, λ_g. The spacing of the re-imaged grating fringes is adjustable by changing the original mask spacing and/or the magnification of the objective lens. The short pulse length provides a wide operating window that can span from tens to hundreds of megahertz, easily controlled by adjusting the mask spacing or the magnification factor. A second (probe) laser is used to measure the perturbation caused by SAW propagation. The beam is focussed on to the sample and returned to a split photo-diode detector, yielding a signal that is sensitive to the slope of the surface. The optical arrangement of the system is shown in Fig. 2(a). In this work the generation laser was of wavelength 1064 nm so as to be well absorbed by the specimens and the detection beam was of wavelength 532 nm in order to maximise the proportion of the beam reflected by the specimen surface back to the optical detector. The sample can be raster scanned to captured the SAW velocity across the specimen surface.

In Fig. 2(b), a polycrystalline sample is shown, where the colour indicates a differing grain orientation. The generation patch is shown by red fringes of light, this is thermo-elastically absorbed by the specimen. This then generates a SAW of fixed wavelength,

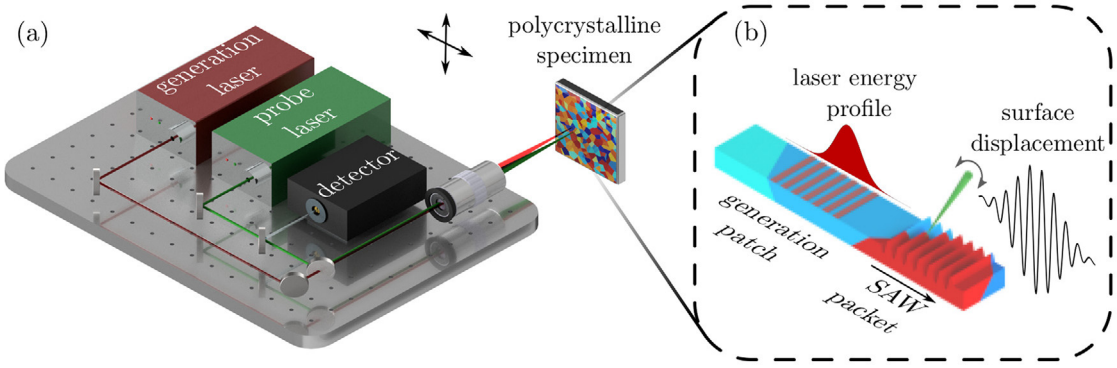

Fig. 2. The SRAS experimental method described in this work. (a) The generation and probe laser beams are delivered to the specimen by the same objective lens and reflected probe light is shown incident at the detector. The grating mask in the generation path is imaged at the specimen surface with adjustable magnification to control the SAW wavelength. (b) Schematic of SAW generation and propagation, (SAW amplitude is exaggerated). The surface perturbation deflects the beam proportionally to the gradient, which is then measured by a split-photodiode detector. The frequency of the wave remains a function of only the properties under the generation patch. (inset waveform) example of measured signal.

that propagates perpendicular to the fringe direction. The generated surface acoustic wave propagates at a frequency, f_s, which is simply determined by the elementary equation $v_s = f_s\lambda_g$, where v_s is the SAW velocity. Rayleigh surface waves are non-dispersive, thus the frequency of propagation does not change once generated; the frequency of the wave packet is a function of the near-surface properties, primarily the elastic response, under the generation patch only and is not affected by grain boundary crossings or variations in the propagation distance. Thus, the SAW velocity can be measured for each generation point across the specimens surface. This method is unlike traditional time-of-flight measurements and is immune to acoustic aberrations [25]. Fig. 1(b) shows the measurement of surface acoustic waves in three grains, one at higher frequency (and higher velocity) and one at lower frequency, the SAW propagates only in directions normal to the grating pattern. Therefore, by rotating the generation patch, SAWs can be propagated at different angles, which allows the anisotropy of the SAW velocity to be probed [26].

The all-optical non-dispersive nature of SRAS avoids the painstaking alignment of a grain centre to the acoustic source [12], without the need for couplant or polydimethylsiloxane film [27]. The high signal-to-noise (SNR) ratio of SRAS allows high fidelity measurements to be made without temporal averaging - this results in multi-megapixel images of the microstructure, which are captured in less than 1 h [23].

Finally, when measuring SAWs, the condition of the surface becomes an important factor to consider. The stress state of a specimen can have a perceptible effect the SAW velocity, origins of this include damage from polishing, annealing [28] or shot-peening [29]. In many metals, the damage layer can extend to a few tens of micrometres, greater than the typical penetration depth of many SAW methods [30]. This is particularity a problem of Brillouin scattering as the working frequencies (>1 GHz) result in a SAW which is extremely sensitive to the surface condition [31]. The acoustic wavelength, and hence penetration depth, of SRAS can easily be varied between $\sim 12-250$ µm. Depending on the wavelength used, the reader should be aware that the derived elastic properties are only representative of the interrogated volume at the surface.

2.6. Examined materials and sample preparation

Three specimens were examined experientially, one face-centercubic pure nickel, one hexagonal-close-packed pure α-titanium and a CMSX-4 nickel alloy specimen. Nickel and titanium are the basis of many pivot engineering alloys throughout aerospace [32] and nuclear applications [33], making them sensible candidates to demonstrate the present technique.

The pure nickel specimen was a single-crystal cylinder, cut with its (001) plane exposed for examination. The titanium specimen was polycrystalline, cut with an exposed face of dimensions 22.5 mm × 12 mm, with several distinct grains contained within this area.

CMSX-4 is a common aerospace alloy, favoured for its combination of high-temperature strength, stiffness and microstructural stability and resistance to fatigue and oxidation/corrosion [34]. The specimen presented in this work was cast in a mould-seed geometry for seeded single crystal growth of a turbine blade, with the imaged specimen cut from the channel section, giving a polycrystalline microstructure. Further detailed information on sample preparation and microstructure can be found in [35]. The CMSX-4 specimen presented in this work was the second in a collection of specimens manufactured at the same time. Specimen A was left in the as-cast state, whilst specimen B was subjected to solution heat treatment. Both A and B were taken from sections through the channel. These specimens are of particular interest as previous reporting had shown good agreement between SRAS results and EBSD for orientation determination in only specimen A, when using literature elastic constant values for CMSX-4 [36]. As described in that work, the same elastic constant values produced a poor orientation result for the heat-treated specimen.

All specimens discussed had their exposed surface prepared by mechanical polishing, leaving the specimen with a mirror-like finish (this is essential for the implementation of the SRAS instrument used in this work). Electron back scatter diffraction was used to image the polycrystalline microstuctures and orientation prior to SRAS scanning. The grains of both polycrystalline specimens used for this study were relatively coarse (>500 µm), this is significantly larger than the spatially resolution of the system, 100 µm), meaning the studied grains were well-resolved.

3. Sensitivity modelling

3.1. Influence of elasticity on ultrasonic velocity

The first step in extending the inversion method to the determination of elastic constants, is a sensitivity analysis relating changes of elastic constants to the SAW velocity. Fig. 3(a)–(c) shows the change in SAW velocity on the {111} plane in pure Ni for the three elastic constants independently perturbed by ±20 GPa. The first point to note is that the effect of C_{11} is the inverse of C_{12}, this is suggestive of interdependence between these constants. Further-

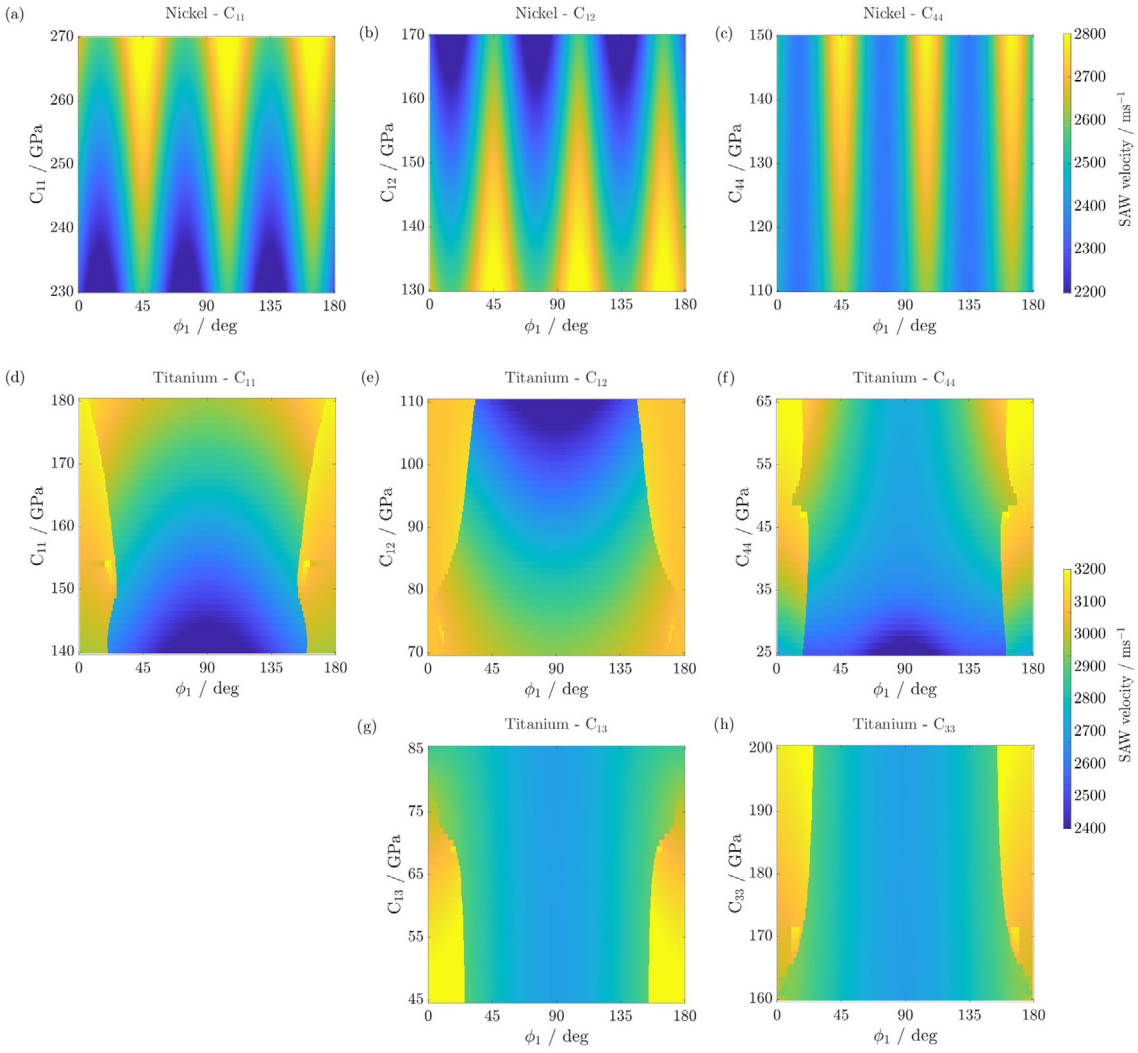

Fig. 3. (a)–(c) present results in cubic Ni. The change in SAW velocity across the {111} plane for perturbations in the elastic constants (a) C_{11}, (b) C_{12}, (c) C_{44} over a range of 40 GPa. It is important to note the dependence between C_{11} and C_{12}, simply perturbing C_{11} and C_{12} in equal and opposite directions (i.e. $C_{11} \Uparrow$, $C_{12} \Downarrow$ by 10 GPa) results in a near identical SAW velocity. (d) - (h) present results for hexagonal Ti on the plane $\phi = 45^\circ$, for perturbations in each of the five independent elastic constants over a range of 40 GPa. $\phi = 45^\circ$ is selected as it has both RSAW and PSAW components. (d) C_{11}, (e) C_{12}, (f) C_{44}, (g) C_{13}, (h) C_{33}.

more, there is an anisotropy in the velocity change, for example comparing C_{44} at 45° and 70°. Over this range, the change in velocity is in the order of 600 ms^{-1}. The repetition spaced by 60 degrees is due to the six-fold symmetry on the plane {111}, planes near {001} have four-fold symmetry and intermediate planes have two-fold symmetry. These findings are in good agreement with the work of Stoklasova et al., who note that as the SAW has a significant shear component, the shear elastic coefficients, $\frac{C_{11}-C_{12}}{2}$ and C_{44} can be accurately determined by SAW velocity measurement [37].

Fig. 3(d)–(h) shows the change in SAW velocity on the plane $\Phi = 45^\circ$ when varying the five independent elastic constants of titanium, again across a range of ±20 GPa. Titanium is characterised by the presence of the PSAW, which dominates close to the basal plane before giving way to the RSAW as the cut-plane tilts away, $\Phi = 45^\circ$ has been chosen as it exhibits both wave modes. From (d) and (e) again we see that C_{11} is the inverse of C_{12}, in the RSAW regions. However, in the PSAW region varying C_{12} appears to have no impact on the SAW velocity. In the recent work of Zoubkova et al. the authors suggest the measurement of Rayleigh type surface waves is important for accurate determination of the full elastic constant matrix [38]. This is in agreement with the present finds, which suggest measurement of the PSAW represents a route to decouple the elastic constants C_{11} and C_{12}.

This illustrates governing properties for the RSAW and PSAW are different and thus have different interactions with elastic constants. The basal plane is isotropic in hexagonal materials, this means only Euler-Bunge angles ϕ_1 and Φ can be determined by linear acoustic techniques [20]), an important limitation of this work for orientation determination.

The results for C_{13} and C_{33} are given in Fig. 3(g)-(h), respectively. For the RSAW mode both constants exhibit minimal effect on the SAW velocity. In the PSAW region the change becomes more distinct ($\sim 150\,ms^{-1}$ over ±20 GPa). It is also seen that the value of C_{13} and C_{33} changes the position of the mode transition. Given this effectively causes changes in SAW velocity of $\sim 500\,ms^{-1}$ accurately measuring this position is likely to greatly improve the accuracy to which these elastic constants can be determined.

Given the interaction shown in Fig. 3(a),(b) and (d),(e) it is useful to consider the value of $C_{11} - C_{12}$, henceforth referred to as C_Δ to prevent confusion with the plane $C_{11} - C_{12}$, which refers to the $x - y$ space mapped by plotting the value of F_E for a range of values of C_{11} and C_{12}, with all other elastic constants held constant.

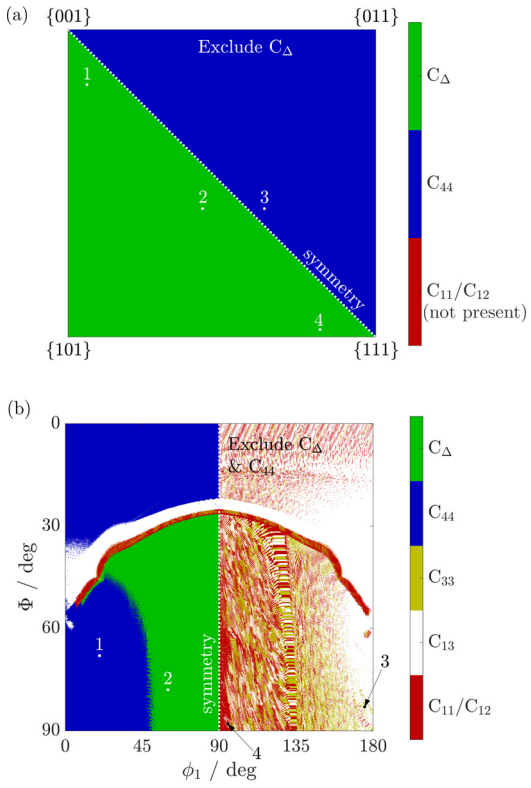

Fig. 4. (a) C_Δ is the elastic constant that causes the greatest change in SAW velocity across the orientation space in Ni. The change in SAW velocity at the four marker positions are 1) 70 ms^{-1}, 2) 140 ms^{-1}, 3) 55 ms^{-1} and 4) 22 ms^{-1}. The change from perturbations C_{11}/C_{12} is not shown but varies between 6 ms^{-1} near {001} and 2 ms^{-1} near {111}. (b) The elastic constant that causes the greatest change across the orientation space in Ti. C_{44} and C_Δ have been excluded for $\phi_1 > 90°$ (line of symmetry). The change in SAW velocity at the four markers positions are 1) 89 ms^{-1}, 2) 76 ms^{-1}, 3) 15 ms^{-1} and 4) 1 ms^{-1}.

C_{11}/C_{12} is used to refer both constants in cases where their behaviour is similar.

Fig. 4 (a) shows the elastic constant, which causes the greatest change in SAW velocity across the orientation space in Ni. Velocity surfaces are symmetric about the indicated line and thus C_Δ can be excluded in the second half to provide information on the succeeding sensitivity. The result is a simple conclusion where the order of sensitivity $C_\Delta, C_{44}, C_{11}/C_{12}$ is constant across all planes. The change in SAW velocity however, remains anisotropic. In short, measuring a plane near {0.5 0.5 1} makes constant determination an easier task than near {001}, as the change in SAW velocity - as a function elastic constants - is greater.

Similarly, Fig. 4(b) shows the elastic constant sensitivity in Ti, across the orientation space. C_Δ and C_{44} are the dominant elastic constants across the orientation space, as seen in the left hand-side of the plot. SAWs in hexagonal crystal structures are symmetric about $\phi_1 = 90°$; C_{44} and C_Δ have been excluded for $\phi_1 > 90°$. The response in this region is harder to interpret, with a chaotic behaviour flipping between C_{11}/C_{12}, C_{13} and C_{33} as elastic constant which causes the greatest change in SAW velocity. In general, directions close to $\phi_1 = 90°$ are sensitive to C_{11}/C_{12}, then give way to C_{13} as $\phi_1 \to 0°$. Grabec et al. have recently studied the elastic constants of tetragonal materials (which belongs to the same crystal family as hexagonal materials) and determined that in addition to the shear elastic coefficients which are well determined in the cubic case, the additional volume-preserving extension term $\frac{C_{11}-C_{12}+2C_{13}-4C_{33}}{6}$ may be easily determined by SAW measurements, again this is in good agreement with the results presented in the present work [39].

In summary, these results demonstrate the underlying anisotropy of the elastic constant influence in SAW velocity. The variation in the SAW velocity, within a useful range of elastic constants, are well within the bounds of typical SAW measurement accuracy at certain angles ($> 100 \text{ms}^{-1}$), but necessitate challenging levels of accuracy at other angles ($< 1 \text{ms}^{-1}$). By sampling various crystalline orientations the sensitivity to each elastic constant can be maximised. Therefore, the inversion algorithm proposed in this work is most effective when using velocity surfaces from multiple grain orientations to ensure some sensitivity to all elastic constants is included.

3.2. Analysis of error and uncertainty

The next step in determining the elastic constants from SAW velocity is to investigate the solution space, understanding this is an invaluable tool for tailoring the search, informing on the accuracy of elastic constant determination and dictating the search range. In general, it is beneficial for the solution space to be concave, with a single global minimum, with large variations in F_E when members of C_{ijkl} are perturbed. Fig. 5(a) shows this to be true in the plane $C_{11} - C_{44}$, the position of the minimum in this plane could be well determined by any simple optimisation algorithm. In contrast, the minimum is poorly defined in the plane $C_{11} - C_{12}$; values along the same diagonal trajectory (where C_Δ remains constant) produce similar values of F_E. This is the impact of the interdependence between C_{11} *and* C_{12}, as shown in Fig. 3.

As shown by Fig. 5(a), the orthogonal $C_{11} + C_{12}$ is therefore the direction with poor sensitivity. This effect can be visualised by looking at two typical velocity surfaces from elastic constant perturbation; Fig. 5(c) where SAWs on the plane (111) for a perturbation in the plane $C_{11} - C_{44}$ (blue line) and the plane $C_{11} - C_{12}$ (red line), of equal perturbation from a nominal value (black line). Clearly, the perturbation in the C_{44} direction is much larger, 102 ms^{-1} on average, than the $C_{11} - C_{12}$ direction where the change is only 2 ms^{-1} on average.

The range over which to search can be estimated by plotting the elastic constants of several cubic materials on a scale normalised by the value of C_{44}. Most materials have several similar literature vales. However, it appears most are tightly spread in the C_Δ direction but can be extremely spread out in the $C_{11} + C_{12}$ direction. $\beta - Ti$ (red diamonds) and Al (blue circles) are notable examples. Whilst not conclusive, this would be typical of measurements which can determine C_Δ but lack the accuracy to determine the specific values of C_{11} and C_{12} along the minimum. Applying the familiar Born stability criterion $C_{11} > C_{12}$ significantly reduces the search space ($E < 0$ region in black). Given this, and the importance of searching close to the plane $C_{11} + C_{12}$, searching in a square grid generates many solutions far way from the minimum and in some cases solutions that are unstable (inset square grid). Instead, a grid tiled around values of C_Δ allows greater refinement of search (inset tilted grid). The Zener anisotropy ratios, α, 0.5, 1 and 2 are indicated by dashed white lines. It is worth remarking the difference between anisotropy where $\alpha > 1$ and $\alpha < 1$. Aside the from the absolute difference in velocity, the shapes of the velocity surface in KCL ($\alpha > 1$) and Ni ($\alpha < 1$) are noticeably different, as the directions of high velocity are 45° out of phase. Care should be taken not to perform the inversion of measured velocity surfaces with modelled surfaces from the other side of $\alpha = 1$ as the incorrect rotation on the plane may be determined. Further information of this style of plot can be found in [40].

In titanium, the solution space of the planes $C_{11} - C_{44}$ and $C_{11} - C_{12}$ is similar to (a) and (b), such that it is not worth reproducing here. Instead, two particularly interesting planes are shown. Firstly, Fig. 5(e) plots the value of F_E for $\Phi = 90°$ in the plane $C_{13} - C_{33}$, note the scale has changed from Fig. 5(a)-(b). Whilst we

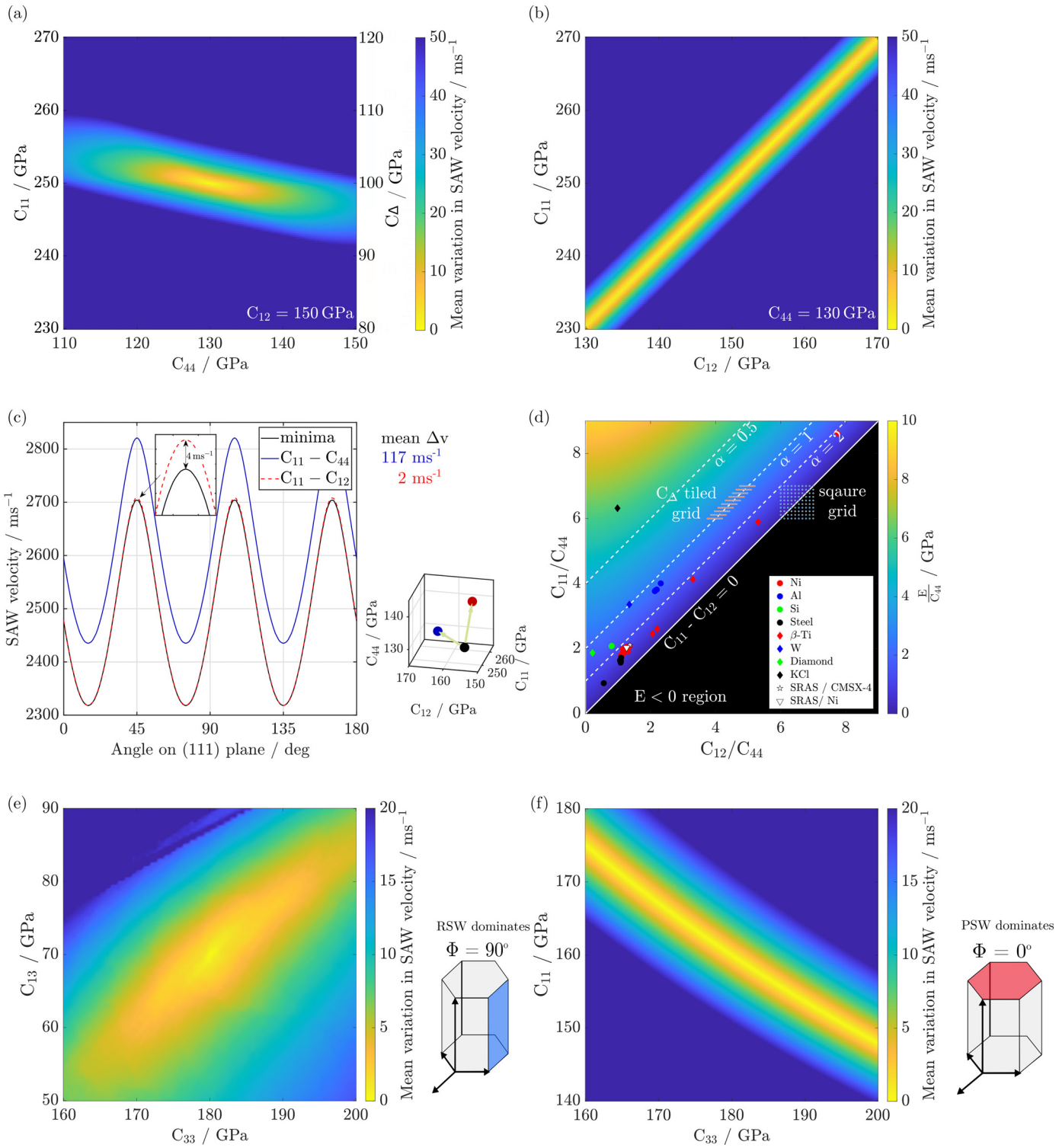

Fig. 5. Examples of elastic constants solution spaces for nickel (a)-(b). (a) The plane $C_{11} - C_{44}$. The minimum is well defined at ($C_{44} = 130$ GPa, $C_{11} = 250$ GPa). (b) The plane $C_{11} - C_{12}$. The minimum is poorly defined at ($C_{12} = 150$ GPa, $C_{11} = 250$ GPa). (c) Comparison of SAWs on the plane (111) for a perturbation in the plane $C_{11} - C_{44}$ (blue line) and the plane $C_{11} - C_{12}$ (red line), of equal perturbation (10 GPa) from the minimum (black line). The relative position of the three elastic constants sets are shown in the inset scatter plot. Perturbations in C_{44} are easier to measure as they cause larger changes in the SAW velocity. (d) Elastic constants of several cubic materials on a normalised scale. The background colorscale is the normalised Young's modulus (E/C_{44}) in the [001] direction and α is the Zener ratio [40]. Several materials appear spread along the diagonal of anisotropy, this is the direction of least sensitivity. Thus, when determining elastic constants a wide range of values along this diagonal should be considered. Examples of the solution space in hexagonal titanium, note the scales have been reduced compared to Ni (d) - (e). (d) The plane $C_{13} - C_{33}$ in the RSAW region. (e) The plane $C_{11} - C_{33}$ the PSAW region, this region has a greater sensitivity to C_{33}, but has a co-dependency on the value of C_{11}. (For interpretation of the references to colour in this figure legend, the reader is referred to the web version of this article.)

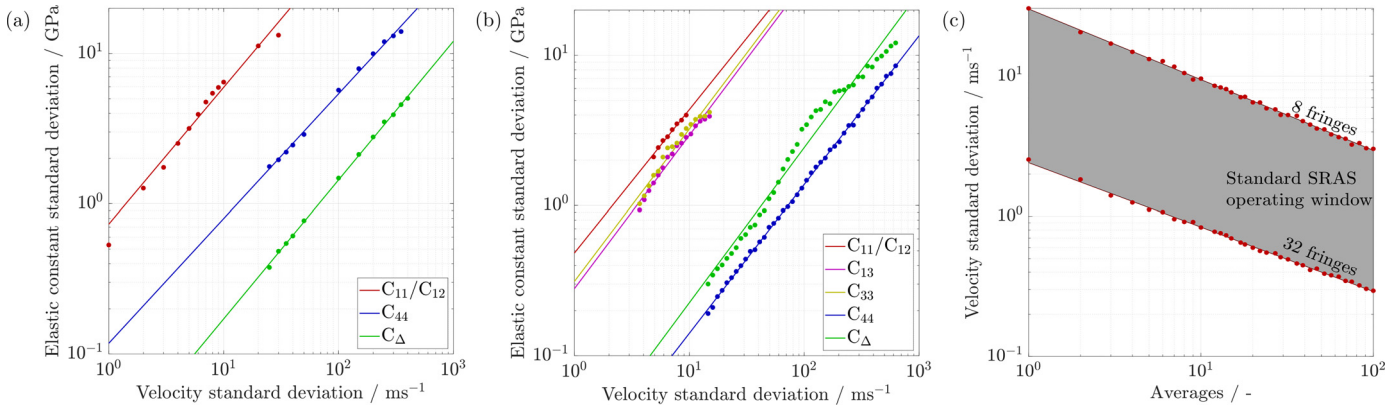

Fig. 6. Simulations of errors in the determination of elastic constants, as a function of velocity standard deviation for pure (a) Ni and (b) pure Ti. (c) provides context to (a) and (b) by illustrating the typically available velocity standard deviation in the SRAS experiment, as a function of signal averages. From (c) it can be seen that a velocity standard deviation of $< 10\,\mathrm{ms}^{-1}$ is readily achievable even in the 8 fringe case (more broadband signal) with few averages (~ 10), this corresponds to a standard deviation of $10\,GPa$ for C_{11} and C_{12} (least sensitive constants) in Ni (approximately 4% and 6.65%, respectively).

see a minimum does exist, the function is weakly concave. Finally, Fig. 5(g) plots the value of F_E for $\Phi = 0^\circ$ in the plane $C_{11} - C_{33}$, this region has a greater sensitivity to C_{33} (Fig. 3(h)) but it has an interdependence on the value of C_{11}, making the minimum poorly defined. To the authors knowledge, this is the first reporting of the solution space in hexagonal crystal systems.

The ability to accurately determine the elastic constants of the specimen is primarily dependent on the instrument accurately measuring the SAW velocity. By simulating the velocity surfaces that would be determined by a range of δv the corresponding errors in elastic constant determination were elucidated. Fig. 6 shows the resulting standard deviation in elastic constant determination as a function of the velocity error standard deviation for (a) nickel and (b) titanium. The experimental availability of these velocity errors is contextualised by Fig. 6(c), showing the expected velocity standard deviation as a function of number of signal averages and fringes in the generation patch. In both materials we see C_{44} and C_Δ is determined most accurately, whilst the interdependency between C_{11} and C_{12} causes significantly more uncertainty. As hypothesised from Fig. 3(f), C_{13} is slightly easier to determine than C_{33}. Reducing the standard deviation in the determination of all elastic constants to below 1 GPa is practically achievable if > 100 averages can be used, allowing the elastic constants to be determined with meaningful accuracy.

4. Experimental results

4.1. Nickel and CMSX-4 alloy

The following section presents the results of elastic constant and crystallographic orientation determination in three real-world specimens. We firstly present the inversion of a velocity surface (Fig. 7(a)) of a Ni single crystal specimen on the (001) plane. Elastic constant values for pure Ni are well established in published literature and thus provides a useful basis for validating the inversion method. The determined crystallographic plane is {001}, and elastic constants calculated by inversion are in good agreement with the prior literature, Fig. 7(b) - results from this specimen are indicated by ▼ markers.

The previous result, in single crystal Ni, has demonstrated the technique with a single high quality velocity surface in a specimen with well characterised elastic properties. A more complex Ni alloy is now considered, using a greater number of grains but lower quality velocity surfaces. Two CMSX-4 polycrystalline specimens were fabricated (with one annealed and one left in the 'as-built' state) and then scanned by SRAS, with the SAW velocity measured in 18 directions at an interval of 10°. The orientation result of the 'as-built' specimen has previously been reported [36], and showed good agreement to EBSD, using literature elastic constants. The annealed specimen (studied below) is of particular of interest to the present work as the original orientation result showed poor agreement to EBSD, suggesting an error in elastic constants.

The seven grains indicated in Fig. 7(g(i))) were selected for the inversion process as these had unique orientations and a large number of pixels with good SNR. The waveforms from each pixel in these grains were then averaged (each grain had at least 1000 pixels once boundary regions and locations with poor SNR ratio were excluded). From Fig. 7(b) (results from this specimen are indicated by ★ markers), the calculated elastic constants are within the reported range for CMSX-4; C_{11} and C_{12} are particularly in good agreement with the measurements of Amulele et al. for CMSX-4 [41].

However, the calculated value of C_{44} is $\sim 8\,GPa$ lower than reported values. Mendik et al. found that alongside the impact of surface condition and residual stress, annealing a sample changes the measured SAW velocity and lower the values of C_{44} measured [30]. Annealing of the specimen is the only difference between this specimen and that previously reported with good orientation agreement using literature elastic constants, and therefore the probable source of discrepancy in C_{44}.

Example results of the inversion process for grain 5 are shown in Fig. 7(c), directions with high SNR (such as 90°) had a smaller velocity standard deviation, this was due to the anisotropy in the amplitude of the SAW [42]. The mean difference between the measured data and inversion is $19\,\mathrm{ms}^{-1}$, compared to $78\,\mathrm{ms}^{-1}$ for the literature elastic constants in this grain.

Bearing in mind the variation in SAW velocity due to elastic constant perturbation is anisotropic across a plane (see Fig. 3), it is useful to compare the measured propagation directions to the sensitive directions, as when measuring only 18 directions it may be possible to miss propagation directions that cause large changes in the SAW velocity, for a given elastic constant. Fig. 7(d) plots the angle measured velocity surfaces against the change in velocity for a perturbation in C_{44} of 10 GPa for seven planes, corresponding to those used in the inversion. Aside from grain 3, the velocity surface was measured in a region with a change in velocity greater than $50\,\mathrm{ms}^{-1}$. This suggests the inversion should be sensitive to C_{44} and the calculated value of 119 GPa is accurate.

Fig. 7 (e) shows the orientation result of the SRAS inversion compared to the EBSD dataset and the orientation calculated from literature values for CMSX-4 elastic constants. In general, the EBSD data are in much better agreement with the orientation calculated

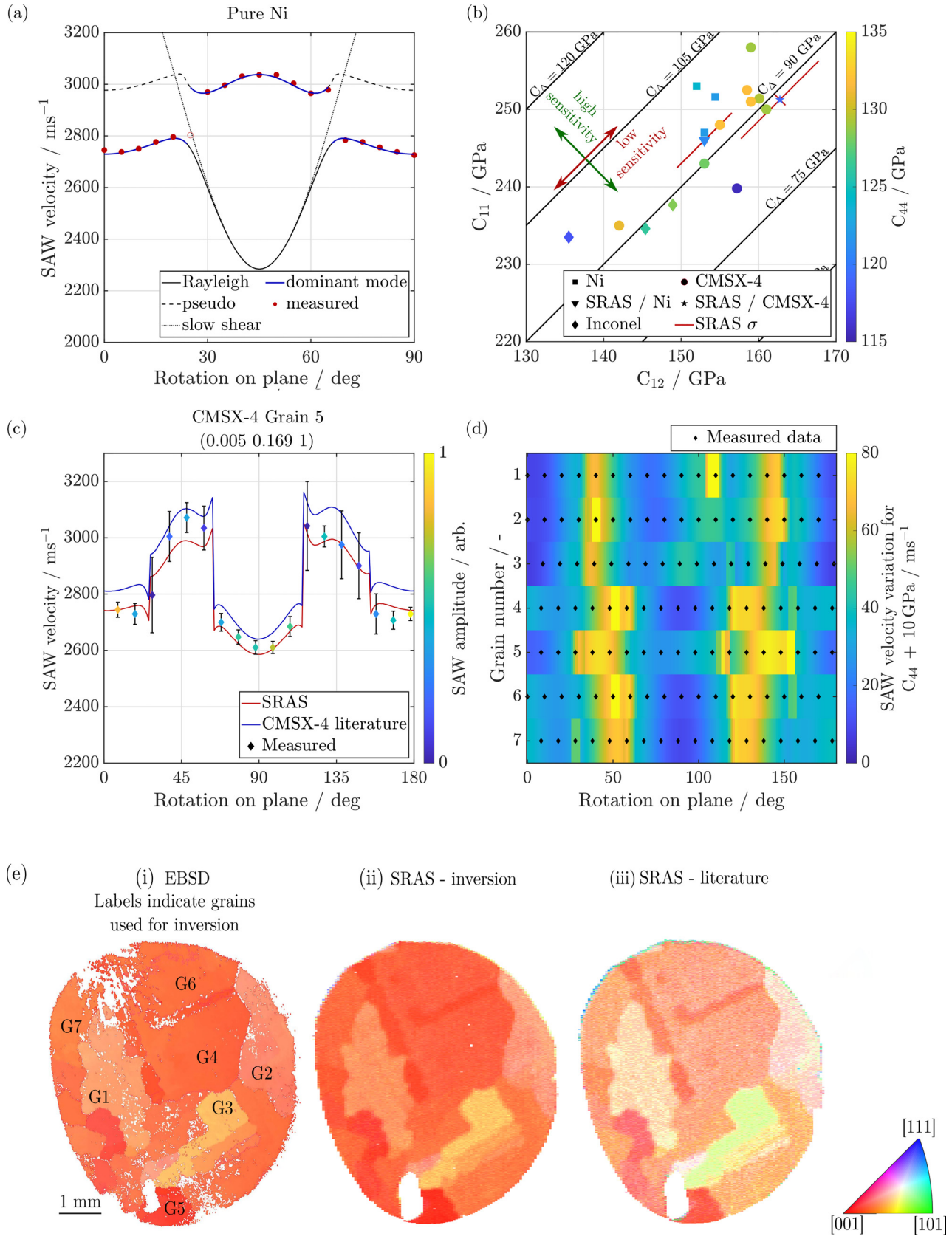

Fig. 7. (a) Measured data for single crystal Ni specimen, with fitted data superimposed. The measured data-point $\sim \phi_1 = 25^\circ$ has been excluded from inversion as this occurs at the transition between wave modes as shown. (b) The elastic constants of Ni and Ni-alloys. Both experimental datasets show good agreement to existing values. Red bars indicate the expected standard deviation in elastic constants determined in this work. The SAW inversion is particularity sensitive to the value of C_Δ. (c) Velocity surface from grain 5 compared to the velocity surfaces (red-line) from SRAS inversion and literature value of elastic constants. The colourscale of the measured data indicates the relative amplitude of the SAW in the given direction. Error bars indicate the standard deviation of the measurement across the pixels used for the inversion. (d) Plot of the velocity variation as a function of 10 GPa perturbation in C_{44}, for the 7 grains used as inputs for the inversion and the position of the 18 ultrasonic measurements on each grain. In all grains except 3, several measurements have been taken at angles with high sensitivity. (e) Comparison of the inverse pole figures for the CMSX-4 specimen, from (left to right) EBSD, SRAS using inversion elastic constants and SRAS using existing elastic from literature. Numeric labels in the EBSD data indicate the grains used in the inversion process. The elastic constants calculated by the SRAS inversion in this work have significantly improved the orientation result, relative to the EBSD dataset. (For interpretation of the references to colour in this figure legend, the reader is referred to the web version of this article.)

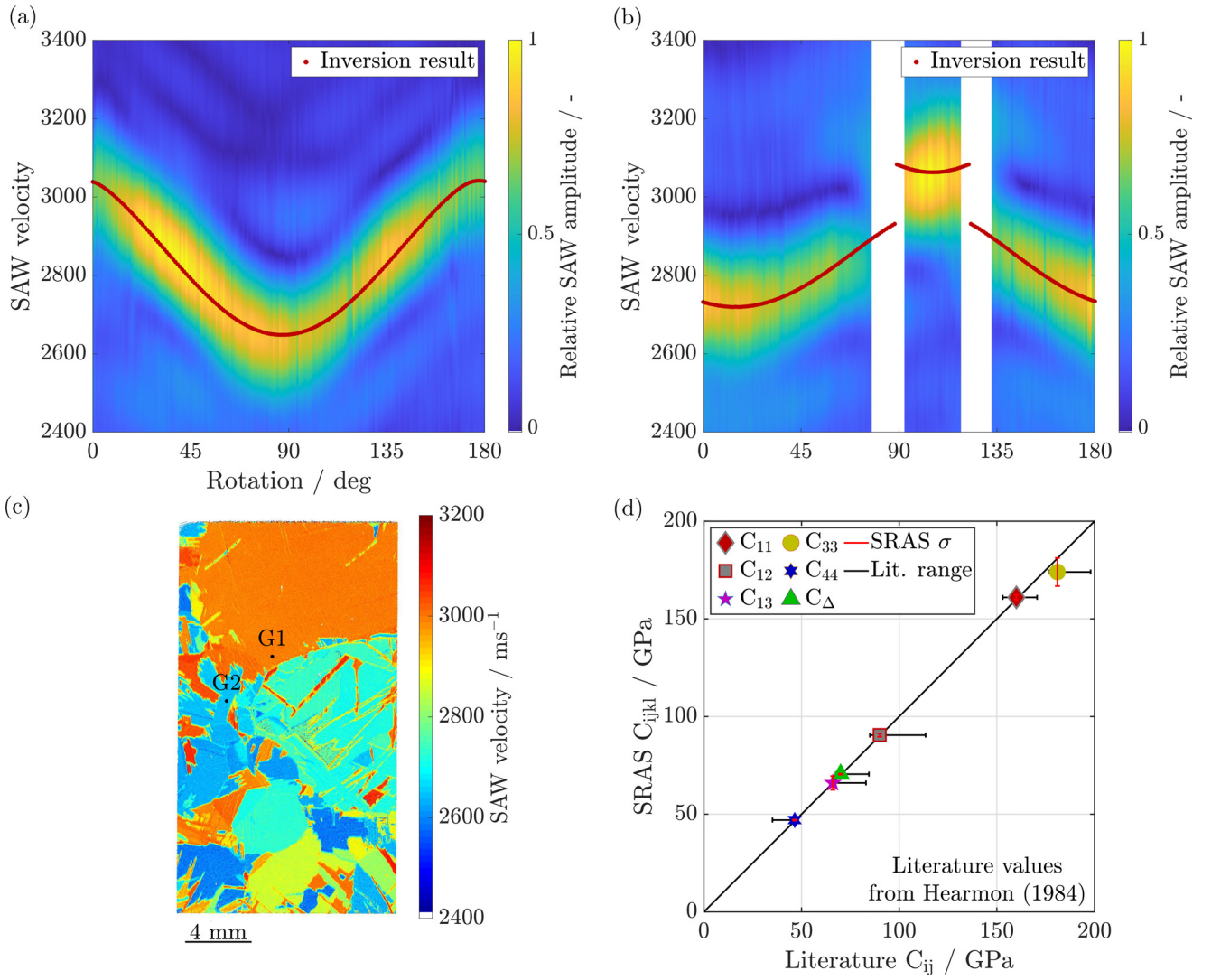

Fig. 8. (a) Measured velocity surface in Grain 1, with fitted result from inversion superimposed, calculated to be $\phi = 66°$. (b) Measured velocity surface in Grain 2, with fitted result from inversion superimposed, calculated to be $\phi = 39°$. The orientation was determined within 1° of EBSD in both cases, areas shown in white indicate where data was omitted from inversion, due to the uncertainty of the mode transition. (c) Single direction SRAS velocity map of whole specimen surface, G1 and G2 indicate the two grains used for inverse analysis. (d) Comparison of elastic constants determined by SRAS and literature values, for Ti. Red bars indicate the expected standard deviation on each elastic constant from SRAS inversion. Black bars indicate the range of values found in prior literature. All constants fall within the range found in literature and all except C_{33} show good agreement with the values of Hearmon [43].

in this work. Considering the EBSD data have not been used as an input to the inversion and is generally considered the benchmark for crystallographic orientation calculation this helps confirm the validity of the new elastic constant set for this specimen. For Φ, the rotation between (001) and (111), the disagreement between inversion elastic constants and EBSD was 1.3°, compared to 5.9° for the literature values. For ϕ_2 the discrepancies were 6.9° and 13.1°, respectively. Given the values of C_Δ, C_{11} and C_{12} match those found in literature, the updated value of C_{44} has clearly been crucial in improving the orientation determination.

4.2. Pure titanium

Determination of the elastic constants in hexagonal materials is more complex as the search space becomes significantly larger due to five independent elastic constants. Furthermore, from Figs. 3(g)-(h) and 5(d) the SAW velocity has a weak sensitivity to the two additional constants C_{13} and C_{33} across much of the orientation space. To demonstrate the proposed method, a polycrystalline titanium specimen was scanned using SRAS, Fig. 8(c) shows the single direction SRAS velocity map and indicates the two arbitrary grains targeted for the inversion. The inversion result and calculated orientation are shown in Fig. 8(a) and (b) for grains 1 and 2, respectively. The crystalline plane, ϕ, of the two grains was calculated as 66° and 39°, respectively, within 1° of the mean EBSD result from the grain in both cases. The determined elastic constants show good agreement with existing literature values, Fig. 8(d). In all cases, the elastic constants fall within the range found in prior literature, and agree particularly well with oft-quoted values determined by Hearmon [43].

In the case of C_{33} there is a discrepancy of ~6%. In Grain 1 (Fig. 8(a)), the sensitivity in C_{33} comes from the RSAW velocity around $\phi_1 = 0/180$, which in the measured data are relativity lower amplitude than at $\phi_1 = 0°/180°$. In Grain 2 (Fig. 8(b)), the position of the mode transition provide the sensitivity to C_{33}, however data around this position this was omitted from the inversion.

5. Discussion

Combined improvements in hardware and algorithm efficiency have allowed a brute-force approach, as used in this work, to become a viable method for the first time. The calculation of a

Table 1
Forward model search resolution for inversion of SAW velocities in CMSX-4 specimen.

Parameter	Resolution
Coarse search	
(hkl)	0.1 to (011) to (111)
C_{44}	1 GPa over 30 GPa
C_{Δ}	0.5 GPa over 10 GPa
Computation time	6 h
fine search	
(hkl)	0.05 to (011) to (111)
C_{44}	0.5 GPa over 8 GPa
C_{11}	0.5 GPa over $C_{\Delta} \pm 4\,GPa$
C_{12}	0.5 GPa over $C_{\Delta} \pm 4\,GPa$
Computation time	16 h

single velocity plane now takes $\sim 5\,s$ at a velocity resolution of $2\,\mathrm{ms}^{-1}$, quoted speeds are for an Intel® i9-10900X @ 3.70 GHz. The generation of forward models and the inversion are both suited to parallel computation, allowing modern multi-core hardware to be leveraged. As a demonstration of the computational demand, Table 1 tabulates the search parameters and computation time for the inversion of the CMSX-4 specimen studied in this work (using the pc described above). The brute-force method has proved attractive given the local minimum and weakly concave shape in the $C_{11} - C_{12}$ plane, mitigating previous issues with optimisation solvers [12].

The standard deviation of elastic constants given in Fig. 6 should be considered a lower-bound of the errors achievable without further modification to the method. Firstly, these errors are dependent on capturing the velocity surface at 180 uniformly incremented propagation directions, reducing this will reduce accuracy. Elastic constant standard deviations expected when using 18 measurement angles, as in the present work, were calculated in this fashion and included with experimental results above. Furthermore, given that the acoustic generation mechanism relies on thermoelastic expansion, we would expect to see some temperature change from the pulsed laser. Simple finite-element modelling estimates the resultant temperature rise in Ti is $< 1\,^{\circ}\mathrm{C}$. Experimental data presented in this work are spatially over-sampled - a given location on the specimen is exposed to multiple laser pulses, therefore the build up in temperature from successive pulses of the generation laser must be considered, this is estimated to be $2 - 3\,^{\circ}\mathrm{C}$, again by finite-element modelling. To give these values context, an increase in specimen temperature of $2^{\circ}\mathrm{C}$ reduces the three cubic elastic constants [44] in turn slowing the SAW velocity by $\sim 10\mathrm{ms}^{-1}$ in CMSX-4 on average [45]. Enacting rigorous temperature control of the specimen during the SRAS experiment will be required to realise improved accuracy.

Finally, in most crystalline materials, certainly in the nickel and titanium specimens studied in this work, several surface wave modes can propagate. In the single crystal Ni and Ti results presented, velocity measurements near the mode transition have been excluded as the current method of discriminating between the modes is somewhat imprecise and leads to uncertainty in the location of these transitions on the plane. In future, coupling the forward model with a finite-element model to calculate the wave mode displacements will further improve the inversion accuracy.

The current implementation of SRAS allows rapid high resolution velocity maps to be acquired by prioritising raster scanning. This has limited the present work to either several grains with few angular measurements or detailed angular measurements in few grains. Making adjustments to the instrumentation to prioritise angular scanning will allow high velocity resolution velocity surfaces to be captured in many grains, with the expectation this would further improve the accuracy in elastic constant determination. Experimental data in this work have been captured at 18 propagation directions with single-shot measurements, optimal parameters for minimising scan time but increases the errors in elastic constant and orientation determination. By using temporal averaging and scanning a greater number of directions, the accuracy of determination can further be improved.

The grain size in all of specimens studied in this work are relativity large (mm-scale). For this proposed method to operate grains must be spatially resolved by the experimental system. Presently, the spatial resolution of the experimental system is $\sim 50\,\mu m$. This covers a wide range of relevant materials and processing routes. However, we envisage the spatial resolution can be further improved by a factor of ~ 10 through minor changes to the optical imaging system, making the proposed method applicable to a wider range of materials.

6. Conclusions

We have presented a measurement and inversion method using SAW velocity measurements to determine the orientation and elastic constants in crystalline specimens, with experimental examples in pure Ni (cubic), Ti (hexagonal) and the Ni-alloy CMSX-4. The determined elastic constants in CMSX-4 are estimated to have associated standard deviations of 2 GPa for C_{44} and 10 GPa for C_{11} and C_{12} (although the value of C_{Δ} is found with a standard deviation of 1 GPa). The final orientation result showed good agreement with EBSD data from the specimen, significantly improved from the orientation result when using literature values for CMSX-4 elastic constants rather than the output of the SRAS inversion. This highlights that aside from determining the elastic constants, the full inversion algorithm has the benefit of making the established orientation inversion process more robust, by removing the dependency on literature values for elastic constants. To close, possible sources of error and future improvements to the methodology were discussed.

As such, the present work establishes the general methodology as an exciting new characterisation tool to non-destructively identify the orientation and single crystal elasticity matrix from polycrystalline specimens. The techniques demonstration on the representative samples with simpler microstructure implies the methodology's wider applicability for novel and previously unmeasurable alloys.

Looking forward, SRAS and other SAW localisation techniques are attractive tools for elasticity measurements as they can be used with polycrystalline specimens of unknown orientation whilst having have spatial and velocity resolutions that can be tweaked to achieve the required accuracy across a wide range of specimens. Drawing together these capabilities promises a flexible tool for measuring the elastic properties across a wide range of materials - supporting future novel research in material sciences.

Declaration of Competing Interest

The authors declare no competing interests.

Acknowledgements

This work was supported by the Engineering and Physical Sciences Research Council [grant numbers EP/L022125/1 (through the UK Research Centre in Nondestructive Evaluation) and EP/S013385/1]. The authors also thank The Royal Society for the provision a travel grant IEC\R3\170081 which aided this work.

The authors acknowledge John W. Aveson and Howard J. Stone of The Department of Materials Science & Metallurgy, University of Cambridge for provision of the CMSX-4 specimen and EBSD data.

Table A1
Review of existing acoustic approaches to measure elasticity and crystallographic orientation.

Technique name	Measurand	Polycrystalline materials	Det. of crystallographic orientation	Simultaneous determination	Experimental specifications	Ref
Spatially resolved acoustic spectroscopy	SAW	✓	1°	✓*	$> 10\,\mu m$ grain diameters	[22]
Line focus acoustic microscopy	SAW	✓	×	×	immersion tank, known orientation and geometry	[46]
SAWP'DMS TDTR'MODEL	SAW	✓	×	×	PDMS film applied to sample, identified grain boundaries	[4]
Acoustic reflection	SAW	×	1° (rotation only)	×	immersion tank, Schlieren imaging	[47]
Scanning acoustic microscope	SAW	✓	✓	✓	large grains, liquid couplant layer	[48]
Acoustic spectro-microscopy	SAW	✓	✓	✓	liquid couplant layer, > 1 mm grain diameters	[12]
Impulse stimulated scattering method	SAW	✓	✓	✓	Similar to SRAS	[49]
Brillioun scattering	SAW, L, S	✓	✓	✓	high frequencies (>1 GHz) give sensitivity close to surface	[50]
Point-source method	L, S	×	✓	×	small excitation area, complex wavefield data	[51]
Ultrasonic bulk wave	L, S	×	✓	×	Precise orientation of crystal axis	[6]
Resonant ultrasound spectroscopy	SW	×	×	×	parallelepiped or similar	[52]
Resonant ultrasound spectroscopy - Baysian method	SW	×	2°	✓	parallelepiped, geometry measured to < 0.1%	[52]

SAW: surface acoustic wave, S: shear bulk wave, L: longitudinal bulk wave, SW: standing wave. * Present work Sensitivity and errors are noted where published results are available, in many cases such information has yet to be reported.

Appendix A. Ultrasonic measurement techniques for elasticity and orientation

Appendix B. Elastic constants

Values of elastic constants for various cubic and hexagonal materials are given in Tables B.3 and B.4, respectively. Values are reproduced as given in the original literature. Where possible, uncertainties and errors are listed, however to-date many studies have omitted these values. Where error bounds are given these are often the error associated with the measurement of the direct property, offered with the caveat that the errors in the final calculation of the elastic constants will be no less than the initial measurement error.

It should also be noted, that in many cases these constants are derived from measurement of the compliance matrix, S_{ijkl}, rather than stiffness matrix, C_{ijkl}, as this is accessible though mechanical testing. However, as reported by Hearmon, recovering C_{ijkl} by the inversion of S_{ijkl} is highly sensitive to measurement errors, leading propagation of large errors in the final elastic constants [53]. For example, a measurement error of just 2% in the compliance values can result in a deviation of over 10% for the elastic constants. For materials with $C_{12} > 0$, inversion of the stiffness matrix to recover the compliance matrix has more tolerable errors.

Unfortunately, the tools for testing the validity of elastic constants extend to only the checking the stability criterion for the crystal. The eponymously named Born criterion for cubic crystals [75]:

$$C_{11} - C_{12} > 0, \qquad C_{11} + 2C_{12} > 0, \qquad C_{44} > 0$$

Table B1
Experimentally derived elastic constants (GPa) of various cubic materials from existing literature.

Material	C_{11}	C_{12} GPa	C_{44}	Notes on errors	Ref
Cubic					
Aluminium	108.2	62.3	28.4	calculated from compliance	[54,55]
	107.3	60.08	28.3	> 0.5%, particularly C_{12}	[56]
Nickel	**246 ± 3.5**	**153 ± 3.5**	**121 ± 1**	-	*
	247	153	122		[54]
	251.6	154.4	122	> 0.5%, particularly C_{12}	[57]
	252.8 ± 2	152 ± 3	123.8 ± 1	propagated from measurement errors	[58]
CMSX-4	**251.5 ± 5**	**163 ± 5**	**119 ± 1**	-	*
	251	159	132	-	[59][A]
	248	155	132	-	[59][B]
	258	159	129	likely ≥ 2%	[41]
	243 ± 2	153 ± 2	128 ± 1	errors are FWHM of the minimisation function	[59]
Silicon	168	66	84	≥ 5%	[60]
	165.779 ± 0.05%	63.9365 ± 0.2%	79.6346 ± 0.05%	-	[61]
	165.64	63.94	79.51	errors expected to be similar to [61]	[62]
Tungsten	512.57	205.82	152.67	calculated from compliance in	[63]
	500.85	198.60	162.67[C]	calculated from compliance in	[64]
	521.48 ± 0.2%	201.01 ± 0.2%	158.50 ± 0.2%	estimated	[65]

*Values determined in this work are shown in **bold**. [A] Reported to the author in personal communication by W. Hermann.
[B] Reported to the author in personal communication by V. Alberts.
[C] Likely to be misprint and should be 152.67 GPa.

Table B2
Experimentally derived elastic constants (GPa) of various hexagonal materials from existing literature.

Material	C_{11}	C_{12}	C_{13}	C_{33}	C_{44}	Notes on errors	Ref
Hexagonal							
Magnesium	$59.4 \pm 0.7\%$	$25.61 \pm 1.8\%$	$21.44 \pm 1.8\%$	$61.6 \pm 0.7\%$	$16.4 \pm 0.7\%$	propagated from measurement errors	[66]
Titanium	$\mathbf{161 \pm 0.6}$	$\mathbf{90.5 \pm 0.5}$	$\mathbf{66 \pm 1.8}$	$\mathbf{174 \pm 3.6}$	$\mathbf{47 \pm 0.3}$	-	*
	$154.0 \pm 0.5\%$	86.0	67.3	$183.0 \pm 0.5\%$	$46.7 \pm 0.5\%$	larger errors for C_{12} & C_{13}	[6]
	160 ± 5	90 ± 4	66 ± 3	181 ± 2	46.5 ± 0.4	standard deviation from three repeats in	[43]
	163.6	92.3	67.92	185.2	47.05	tabulated from graph in [67]	[68]
	$162.4 \pm 0.2\%$	92	69.7 ± 0.8	$180.7 \pm 0.2\%$	$46.7 \pm 0.2\%$	$C_{12} \geq 0.2\%$	[69]
Ti-6Al-4V	136.0	78	68.0	163	40	fitted to experimental mechanical testing	[70]
	$141 \pm 3\%$	$76.9 \pm 3\%$	$57 \pm 3\%$	$163 \pm 3\%$	$48.70 \pm 3\%$	-	[46]
	170.0	92.0	70.0	192.0	52.0	inverted from diffraction elastic moduli	[71]
Zinc	177.6	24.0	60.2	74.0	39.8	Calculated from compliance in [72]	[73]
	163.5	17.1	41.5	55.3	39.8	Calculated from compliance in [72]	[73]
	$163.68 \pm 0.5\%$	$36.4 \pm 2\%$	$53.0 \pm 5\%$	$63.47 \pm 0.5\%$	$38.79 \pm 0.5\%$	-	[74]

*Values determined in this work are shown in **bold**.

and later extended for other crystal systems [76], including hexagonal:

$$C_{11} > |C_{12}|, \qquad C_{33}(C_{11} + C_{12}) - 2C_{13}^2 > 0$$
$$C_{11}C_{13} - C_{12}^2 > 0, \qquad C_{44} > 0.$$

Alers and Neighbours used this approach to detect errors in reported elastic constants for brass and gold [76]. All of the constants listed above satisfy the stability conditions, beyond that it is impossible to draw further conclusions on their validity. Alongside the advancement of technology to measure elastic constants, tools for validation are also a necessary development.

Appendix C. List of symbols

Symbol	Description
F_E	Figure of merit for elasticity at one pixel
F_O	Figure of merit for orientation at one pixel
F_{EO}	Figure of merit for elasticity & orientation at one pixel
$\overline{F_E}$	Figure of merit for elasticity ensemble for whole specimen
N_g	Number of measured grains
v	Measured SAW velocity (ms^{-1})
C_{ij}	Elasticity matrix in Voigt notation (GPa)
I	Binary matrix of calculated velocity
A	Measured velocity surface
N_v	Number of bins in velocity scale
S	Overlap matrix
θ	Relative propagation direction of SRAS measurement
(hkl)	Cubic plane in Miller indices
ϕ_1	First Euler angle, defines rotation on the plane
ϕ	Second Euler angle, used in hexagonal to define the plane
σ_v	Standard deviation of velocity measurement (ms^{-1})
W, X, Y, Z	Orientation of maximum overlap for a given C_{ij}

References

[1] M.H. Sadd, Elasticity: Theory, Applications, and Numerics, Academic Press, 2009.
[2] M. Jamal, S. Jalali Asadabadi, I. Ahmad, H.A. Rahnamaye Aliabad, Elastic constants of cubic crystals, Comput. Mater. Sci 95 (2014) 592–599, doi:10.1016/j.commatsci.2014.08.027.
[3] A.G. Every, Determination of the elastic constants of anisotropic solids, NDT E Int. 27 (1) (1994) 3–10, doi:10.1016/0963-8695(94)90003-5.
[4] X. Du, J.-C. Zhao, Facile measurement of single-crystal elastic constants from polycrystalline samples, npj Comput. Mater. 3 (1) (2017) 17, doi:10.1038/s41524-017-0019-x.
[5] M. Simonelli, N.T. Aboulkhair, P. Cohen, J.W. Murray, A.T. Clare, C. Tuck, R.J.M. Hague, A comparison of Ti-6Al-4V in-situ alloying in selective laser melting using simply-mixed and satellited powder blend feedstocks, Mater. Charact. 143 (2018) 118–126, doi:10.1016/j.matchar.2018.05.039. Metal Additive Manufacturing: Microstructures and Properties
[6] J.W. Flowers, K.C. O'Brien, P.C. McEleney, Elastic constants of alpha-titanium single crystals at 25 °C, J. Less Common Metals 7 (5) (1964) 393–395, doi:10.1016/0022-5088(64)90084-0.
[7] M. Tane, K. Yamori, T. Sekino, T. Mayama, Impact of grain shape on the micromechanics-based extraction of single-crystalline elastic constants from polycrystalline samples with crystallographic texture, Acta Mater. 122 (2017) 236–251, doi:10.1016/j.actamat.2016.09.040.
[8] D. Gasteau, N. Chigarev, L. Ducousso-Ganjehi, V.E. Gusev, F. Jenson, P. Calmon, V. Tournat, Single crystal elastic constants evaluated with surface acoustic waves generated and detected by lasers within polycrystalline steel samples, J. Appl. Phys. 119 (4) (2016) 043103, doi:10.1063/1.4940367.
[9] B. Lan, T. Ben Britton, T.-S. Jun, W. Gan, M. Hofmann, F.P.E. Dunne, M.J.S. Lowe, Direct volumetric measurement of crystallographic texture using acoustic waves, Acta Mater. 159 (2018) 384–394, doi:10.1016/j.actamat.2018.08.037.
[10] K.M.M. Tant, E. Galetti, A.J. Mulholland, A. Curtis, A. Gachagan, Effective grain orientation mapping of complex and locally anisotropic media for improved imaging in ultrasonic non-destructive testing, Inverse Probl. Sci. Eng. 0 (0) (2020) 1–25, doi:10.1080/17415977.2020.1762596.
[11] M.R. Cherry, S. Sathish, R. Grandhi, A numerical method for predicting Rayleigh surface wave velocity in anisotropic crystals, J. Comput. Phys. 351 (2017) 108–120, doi:10.1016/j.jcp.2017.09.002.
[12] Y. Xu, T. Aizawa, J. Kihara, Simultaneous determination of elastic constants and crystallographic orientation in coarse-grained nickel by acoustic spectro-microscopy, Mater. Trans., JIM 38 (6) (1997) 536–545, doi:10.2320/matertrans1989.38.536.
[13] S. Pathak, S.R. Kalidindi, Spherical nanoindentation stress–curves, Mater. Sci. Eng. R Rep. 91 (2015) 1–36, doi:10.1016/j.mser.2015.02.001.
[14] A. Vinckier, G. Semenza, Measuring elasticity of biological materials by atomic force microscopy, FEBS Lett. 430 (1) (1998) 12–16, doi:10.1016/S0014-5793(98)00592-4.
[15] Z. Wang, A.D. Stoica, D. Ma, A.M. Beese, Diffraction and single-crystal elastic constants of Inconel 625 at room and elevated temperatures determined by neutron diffraction, Mater. Sci. Eng. 674 (2016) 406–412, doi:10.1016/j.msea.2016.08.010.
[16] J. Mizuki, Y. Chen, K.-M. Ho, C. Stassis, Phonon dispersion curves of bcc Ba, Phys. Rev. B 32 (1985) 666–670, doi:10.1103/PhysRevB.32.666.
[17] H.M. Ledbetter, R.P. Reed, Elastic properties of metals and alloys, I. Iron, nickel, and ironnickel alloys, J. Phys. Chem. Ref. Data 2 (3) (1973) 531–618, doi:10.1063/1.3253127.
[18] G.W. Farnell, Physical Acoustics–Principles and Methods, vol. VI, Academic Press, New York and London, pp. 109–166.
[19] I.A. Veres, T. Berer, P. Burgholzer, Numerical modeling of thermoelastic generation of ultrasound by laser irradiation in the coupled thermoelasticity, Ultrasonics 53 (1) (2013) 141–149, doi:10.1016/j.ultras.2012.05.001.
[20] P. Dryburgh, R.J. Smith, P. Marrow, S.J. Lain, S.D. Sharples, M. Clark, W. Li, Determining the crystallographic orientation of hexagonal crystal structure materials with surface acoustic wave velocity measurements, Ultrasonics 108 (2020) 106171, doi:10.1016/j.ultras.2020.106171.
[21] W. Li, Laser ultrasonic method for determination of crystallographic orientation of large grain metals by spatially resolved acoustic spectroscopy (SRAS), University of Nottingham, Electrical and Electronic Engineering, 2012 Ph.D. thesis.
[22] W. Li, S.D. Sharples, R.J. Smith, M. Clark, M.G. Somekh, Determination of crystallographic orientation of large grain metals with surface acoustic waves, J. Acoust. Soc. Am. 132 (2012) 738–745, doi:10.1121/1.4731226.
[23] R.J. Smith, W. Li, J. Coulson, M. Clark, S.D. Sharples, M.G. Somekh, Spatially resolved acoustic spectroscopy for rapid imaging of material microstructure and grain orientation, Meas. Sci. Technol. 25 (055902) (2014) 1–11, doi:10.1088/0957-0233/25/5/055902.

[24] R. Patel, W. Li, R.J. Smith, S.D. Sharples, M. Clark, Orientation imaging of macro-sized polysilicon grains on wafers using spatially resolved acoustic spectroscopy, Scr. Mater. 140 (2017) 67–70, doi:10.1016/j.scriptamat.2017.07.003.

[25] S.D. Sharples, M. Clark, M.G. Somekh, Spatially resolved acoustic spectroscopy for fast noncontact imaging of material microstructure, Opt. Express 14 (22) (2006) 10435–10440, doi:10.1364/oe.14.010435.

[26] Y. Hong, S.D. Sharples, M. Clark, M.G. Somekh, Rapid measurement of surface acoustic wave velocity on single crystals using an all-optical adaptive scanning acoustic microscope, Appl. Phys. Lett. 83 (16) (2003) 3260–3262, doi:10.1063/1.1621091.

[27] D. Li, P. Zhao, J.-C. Zhao, D.G. Cahill, Generation and detection of gigahertz surface acoustic waves using an elastomeric phase-shift mask, J. Appl. Phys. 114 (14) (2013) 143102, doi:10.1063/1.4824101.

[28] P.D. Warren, C. Pecorari, O.V. Kolosov, S.G. Roberts, G.A.D. Briggs, Characterization of surface damage via surface acoustic waves, Nanotechnology 7 (3) (1996) 295, doi:10.1088/0957-4484/7/3/020.

[29] A. Ruiz, P.B. Nagy, Laser-ultrasonic surface wave dispersion measurements on surface-treated metals, Ultrasonics 42 (1) (2004) 665–669, doi:10.1016/j.ultras.2004.01.045.

[30] M. Mendik, S. Sathish, A. Kulik, G. Gremaud, P. Wachter, Surface acoustic wave studies on singlecrystal nickel using Brillouin scattering and scanning acoustic microscope, J. Appl. Phys. 71 (6) (1992) 2830–2834, doi:10.1063/1.351013.

[31] S. Sathish, M. Mendik, A. Kulik, G. Gremaud, P. Wachter, Polish-induced surface damage in nickel: scanning acoustic microscopy and Brillouin scattering study, Appl. Phys. Lett. 59 (2) (1991) 167–168, doi:10.1063/1.106008.

[32] B. Choudhury, M. Chandrasekaran, Investigation on welding characteristics of aerospace materials–a review, Mater. Today Proc. 4 (8) (2017) 7519–7526, doi:10.1016/j.matpr.2017.07.083.

[33] I. Bilobrov, V. Trachevsky, Approach to modify the properties of titanium alloys for use in nuclear industry, J. Nucl. Mater. 415 (2) (2011) 222–225, doi:10.1016/j.jnucmat.2011.05.056.

[34] N. Matan, D.C. Cox, P. Carter, M.A. Rist, C.M.F. Rae, R.C. Reed, Creep of CMSX-4 superalloy single crystals: effects of misorientation and temperature, Acta Mater. 47 (5) (1999) 1549–1563, doi:10.1016/S1359-6454(99)00029-4.

[35] J.W. Aveson, P.A. Tennant, B.J. Foss, B.A. Shollock, H.J. Stone, N. D'Souza, On the origin of sliver defects in single crystal investment castings, Acta Mater. 61 (14) (2013) 5162–5171, doi:10.1016/j.actamat.2013.04.071.

[36] W. Li, J. Coulson, J.W. Aveson, R.J. Smith, M. Clark, M.G. Somekh, S.D. Sharples, Orientation characterisation of aerospace materials by spatially resolved acoustic spectroscopy, J. Phys. Conf. Ser. 520 (012017) (2014) 1–4, doi:10.1088/1742-6596/520/1/012017.

[37] P. Stoklasov, T. Grabec, K. Zoubkov, P. Sedlk, S. Krtk, H. Seiner, Laser-ultrasonic characterization of strongly anisotropic materials by transient grating spectroscopy, Exp Mech. 61 (4) (2021) 663–676, doi:10.1007/s11340-021-00698-6.

[38] K. Zoubkov, P. Stoklasov, T. Grabec, P. Sedlk, H. Seiner, Transient grating spectroscopy for complete elastic anisotropy: beyond the measurement of surface acoustic waves, in: 2021 IEEE International Ultrasonics Symposium (IUS), 2021, pp. 1–3, doi:10.1109/IUS52206.2021.9593394.

[39] T. Grabec, P. Sedlk, K. Zoubkov, M. evk, M. Janovsk, P. Stoklasov, H. Seiner, Evolution of elastic constants of the NiTi shape memory alloy during a stress-induced martensitic transformation, Acta Mater. 208 (2021) 116718, doi:10.1016/j.actamat.2021.116718.

[40] D.C. Gazis, R. Herman, R.F. Wallis, Surface elastic waves in cubic crystals, Phys. Rev. 119 (2) (1960) 533, doi:10.1103/PhysRev.119.533.

[41] G.M. Amulele, A.G. Every, S.C. Yates, Acoustic microscopy wall thickness measurements on nickel based superalloy gas turbine blades, in: Review of Progress in Quantitative Nondestructive Evaluation, Springer, 1999, pp. 2001–2007.

[42] A.A. Maznev, A.M. Lomonosov, P. Hess, A.A. Kolomenskii, Anisotropic effects in surface acoustic wave propagation from a point source in a crystal, Eur. Phys. J. B 35 (3) (2003) 429–439, doi:10.1140/epjb/e2003-00295-y.

[43] R.F.S. Hearmon, The elastic constants of crystals and other anisotropic materials, Landolt-Bornstein Tables, III/18, 1154, 1984.

[44] Y.P. Varshni, Temperature dependence of the elastic constants, Phys. Rev. B 2 (10) (1970) 3952, doi:10.1103/PhysRevB.2.3952.

[45] A. Epishin, B. Fedelich, M. Finn, G. Knecke, B. Rehmer, G. Nolze, C. Leistner, N. Petrushin, I. Svetlov, Investigation of elastic properties of the single-crystal nickel-base superalloy CMSX-4 in the temperature interval between room temperature and 1300 °C, Crystals 11 (2) (2021), doi:10.3390/cryst11020152.

[46] J.-Y. Kim, S.I. Rokhlin, Determination of elastic constants of generally anisotropic inclined lamellar structure using line-focus acoustic microscopy, J. Acoust. Soc. Am. 126 (6) (2009) 2998–3007, doi:10.1121/1.3245032.

[47] O.I. Diachok, R.J. Hallermeier, W.G. Mayer, Measurement of ultrasonic surface wave velocity and absorptivity on single-crystal copper, Appl. Phys. Lett. 17 (7) (1970) 288–289, doi:10.1063/1.1653405.

[48] K.-U. Würz, J. Wesner, K. Hillmann, W. Grill, Determination of elastic constants using a scanning acoustic microscope, Z. Phys. B Condens. Matter 97 (4) (1995) 487–492, doi:10.1007/BF01322428.

[49] O. Heczko, H. Seiner, P. Stoklasov, P. Sedlk, J. Sermeus, C. Glorieux, A. Backen, S. Fhler, M. Landa, Temperature dependence of elastic properties in austenite and martensite of Ni-Mn-Ga epitaxial films, Acta Mater. 145 (2018) 298–305, doi:10.1016/j.actamat.2017.12.011.

[50] R. Vacher, L. Boyer, Brillouin scattering: a tool for the measurement of elastic and photoelastic constants, Phys. Rev. B 6 (1972) 639–673, doi:10.1103/PhysRevB.6.639.

[51] A.G. Every, K.Y. Kim, W. Sachse, 2. Point-source/point-receiver methods, in: M. Levy, H.E. Bass, R. Stern (Eds.), Modern Acoustical Techniques for the Measurement of Mechanical Properties, Experimental Methods in the Physical Sciences, vol. 39, Academic Press, 2001, pp. 37–64, doi:10.1016/S1079-4042(01)80085-0.

[52] B. Bales, L. Petzold, B.R. Goodlet, W.C. Lenthe, T.M. Pollock, Bayesian inference of elastic properties with resonant ultrasound spectroscopy, J. Acoust. Soc. Am. 143 (1) (2018) 71–83, doi:10.1121/1.5017840.

[53] R. Hearmon, Temperature dependence of the elastic constants of aluminium, Solid State Commun. 37 (11) (1981) 915–918, doi:10.1016/0038-1098(81)90509-3.

[54] R.F.S. Hearmon, The elastic constants of anisotropic materials — II, Adv. Phys. 5 (19) (1956) 323–382, doi:10.1080/00018732.1956.tADP0323.

[55] E. Goens, Elastizitskonstanten des aluminiumeinkristalls, Ann. Phys. 409 (3) (1933) 233–242, doi:10.1002/andp.19334090302.

[56] J. Vallin, M. Mongy, K. Salama, O. Beckman, Elastic constants of aluminum, J. Appl. Phys. 35 (6) (1964) 1825–1826, doi:10.1063/1.1713749.

[57] K. Salama, G.A. Alers, The composition dependence of the third-order elastic constants of the Cu–Ni system, Physica status solidi (a) 41 (1) (1977) 241–247, doi:10.1002/pssa.2210410129.

[58] J.R. Neighbours, F.W. Bratten, C.S. Smith, The elastic constants of nickel, J. Appl. Phys. 23 (4) (1952) 389–393, doi:10.1063/1.1702218.

[59] X. Zhang, P.R. Stoddart, J.D. Comins, A.G. Every, High-temperature elastic properties of a nickel-based superalloy studied by surface Brillouin scattering, J. Phys. Condens. Matter 13 (10) (2001) 2281–2294, doi:10.1088/0953-8984/13/10/320.

[60] S.C. Prasad, W.A. Wooster, The determination of the elastic constants of silicon by diffuse X-ray reflexions, Acta Crystallogr. 8 (6) (1955) 361, doi:10.1107/S0365110X55001163.

[61] H.J. McSkimin, P. Andreatch Jr, Elastic moduli of silicon vs hydrostatic pressure at 25.0 C and- 195.8 C, J. Appl. Phys. 35 (7) (1964) 2161–2165.

[62] J.J. Hall, Electronic effects in the elastic constants of n-type silicon, Phys. Rev. 161 (3) (1967) 756.

[63] P.W. Bridgman, Some properties of single metal crystals, Proc. Natl. Acad. Sci. 10 (10) (1924) 411–415, doi:10.1073/pnas.10.10.411.

[64] S.J. Wright, T.E. Stanton, The elasticity of pintsch crystals of tungsten, Proc. R. Soc. London Ser.A 126 (803) (1930) 613–629, doi:10.1098/rspa.1930.0030.

[65] C. Anderson, F. Brotzen, Elastic constants of tantalum-tungsten alloys, J. Appl. Phys. 53 (1) (1982) 292–297.

[66] L.J. Slutsky, C.W. Garland, Elastic constants of magnesium from 4.2 K to 300 K, Phys. Rev. 107 (4) (1957) 972, doi:10.1103/PhysRev.107.972.

[67] N. Dumontet, D. Conntable, B. Malard, B. Viguier, Elastic properties of the alpha' martensitic phase in the Ti-6Al-4V alloy obtained by additive manufacturing, Scr. Mater. 167 (2019) 115–119, doi:10.1016/j.scriptamat.2019.03.042.

[68] H. Ogi, S. Kai, H.M. Ledbetter, R. Tarumi, M. Hirao, K. Takashima, Titanium's high-temperature elastic constants through the hcp-bcc phase transformation, Acta Mater. 52 (2004) 2075–2080, doi:10.1016/j.actamat.2004.01.002.

[69] E.S. Fisher, C.J. Renken, Single-crystal elastic moduli and the hcp → bcc transformation in Ti, Zr, and Hf, Physical Review 135 (1964) A482–A494, doi:10.1103/PhysRev.135.A482.

[70] V. Hasija, S. Ghosh, M.J. Mills, D.S. Joseph, Deformation and creep modeling in polycrystalline Ti–6Al alloys, Acta Mater. 51 (15) (2003) 4533–4549, doi:10.1016/S1359-6454(03)00289-1.

[71] J.L.W. Warwick, J. Coakley, S.L. Raghunathan, R.J. Talling, D. Dye, Effect of texture on load partitioning in Ti-6Al-4V, Acta Mater. 60 (10) (2012) 4117–4127, doi:10.1016/j.actamat.2012.03.039.

[72] H.M. Ledbetter, Elastic properties of zinc: a compilation and a review, J. Phys. Chem. Ref. Data 6 (4) (1977) 1181–1203, doi:10.1063/1.555564.

[73] A.W. Hanson, Elastic behavior and elastic constants of zinc single crystals, Phys. Rev. 45 (1934) 324–331, doi:10.1103/PhysRev.45.324.

[74] G.A. Alers, J.R. Neighbours, The elastic constants of zinc between 4.2° and 670°K, J. Phys. Chem. Solids 7 (1) (1958) 58–64, doi:10.1016/0022-3697(58)90180-X.

[75] M. Born, On the stability of crystal lattices. I, Math. Proc. Cambridge Philos. Soc. 36 (2) (1940) 160–172, doi:10.1017/S0305004100017138.

[76] G.A. Alers, J.R. Neighbours, Crystal stability and elastic constants, J. Appl. Phys. 28 (12) (1957) 1514, doi:10.1063/1.1722692.